Monte Carlo Simulation of Effective Dose in Fluoroscopy and Computed Tomography Procedures

by

Jeffrey M. Fenoli

Graduate Program in Medical Physics
Duke University

Date:_____

Approved:

_____
Anuj J. Kapadia, Supervisor

_____
Ehsan Samei

_____
Robert E. Reiman

Thesis submitted in partial fulfillment of
the requirements for the degree of
Master of Science in the
Graduate Program in Medical Physics
in the Graduate School of Duke University

2018

ABSTRACT

Monte Carlo Simulation of Effective Dose in Fluoroscopy and Computed Tomography Procedures

by

Jeffrey M. Fenoli

Graduate Program in Medical Physics
Duke University

Date:_____

Approved:

_____
Anuj J. Kapadia, Supervisor

_____
Ehsan Samei

_____
Robert E. Reiman

An abstract of a thesis submitted in partial
fulfillment of the requirements for the degree
Master of Science in the
Graduate Program in Medical Physics
in the Graduate School of Duke University

2018

Abstract

The overarching goal of this project was to investigate organ dose assessment and variability using Monte Carlo methods to study two areas of medical imaging – fluoroscopy and computed tomography. Namely, these studies were intended to (1) provide estimates of the dose incurred by fluoroscopy-guided spinal injection procedures, and (2) investigate dose heterogeneity in chest and abdominopelvic computed tomography (CT) scans for a range of patient sizes. Fluoroscopy dose estimates were calculated using GEANT4, by recreating the patient procedures of six lumbar-sacral epidural injections. Computed tomography dose was estimated with a GPU-accelerated Monte Carlo package, MCGPU. Both simulations used a library of digital human (XCAT) phantoms, which were previously derived from real-patient CT scans. The fluoroscopy simulations suggest that smaller patients have a higher effective dose per dose area product, and the overall results agreed with previous experimental measurements. Variation of absorbed dose within a given organ was calculated for chest and abdominopelvic CT protocols. It was found that the 95th percentile dose can be over 11 times the mean organ dose in pediatric and adult phantoms. Furthermore, if the organ dose is calculated using only voxels within the beam or all the voxels within an organ, the result can change the result by a factor of 8. The change in dose was found to be higher for organs that have smaller fractions within the beam. Several models of

tissue-weighted dose were also investigated, following similar methods to those used for effective dose. It was found that these tissue-weighted dose calculations can vary by up to 13% depending on whether the out of field dose is included. We also found that the results were not significantly affected by the pitch or projections per rotation. The results have shown that dose-volume details may be hidden by average dose estimates and suggested the need to consider intra-organ dose heterogeneity in CT dose calculations, particularly in the case of sensitive tissues (e.g., bone marrow) and populations (e.g., pediatric).

Dedication

This work is dedicated to my aunt Catherine – her remarkable kindness and caring lives on through her friends and family.

Contents

List of Tables

List of Figures

Acknowledgements

I would like to acknowledge all my colleagues in the medical physics graduate program at Duke University. Their friendship and support have been invaluable resources. I also want to thank members of the Carl E. Ravin Advanced Imaging Laboratories: Paul Segars, for his expertise and development of XCAT phantoms; Shobhit Sharma for his work with MCGPU and Monte Carlo programming and discussions; Brian Harrawood for his continued support with computing and programming; Jocelyn Hoye for her help with GEANT4 simulation setup; Wanyi Fu for her help with XCAT phantoms, PENELOPE simulations, and scanning protocols; and Ehsan Abadi for his calculation of bow-tie-filtered CT spectra.

1. Introduction

In the US, medical imaging continues to be one of the largest sources of radiation exposure. The National Council on Radiation Protection and Measurements (NCRP) report 160, estimates that as much as 48% of our radiation exposure, comes from medical procedures.[1] With an increasing number of imaging procedures performed each year, it becomes important to characterize the ways in which radiation interacts with the human body. One of the most accurate methods for estimating dose involves using so-called Monte Carlo simulations. This technique involves running simulations of individual photons, where probabilistic interactions are assigned weights and random number generators determine the outcomes. Using current technologies, it is possible to simulate tens of millions of photons (or histories) in the matter of hours or less. With this number of histories, the statistical uncertainty of organ doses can be as low as 1%. In these cases, the limiting factor is no longer the statistics, but rather the proper simulation parameters and design. In this work, we investigated two cases for the application of Monte Carlo methods in medical imaging. First, we examined the dose from fluoroscopic imaging used in spinal injections. This study was the first to apply Monte Carlo methods and human phantoms to simulate lumbar spinal injection fluoroscopy. In the second half of this work, we used GPU-accelerated Monte Carlo simulations to study the spatial

distribution of dose within organs for helical computed tomography scans as well as its effect on tissue-weighted dose quantities, similar to effective dose.

2. Patient-specific Monte Carlo dose estimation for fluoroscopy-guided lumbar spine injection procedures

2.1 Introduction

It has been reported that over 80% of adults will experience low back pain at some point in their lives and nearly a quarter of adults will experience chronic low back pain.[2] Even more striking is the fact that low back pain is currently the leading global contributor to years lived with disability.[3] While there are a variety of treatment options available, many of the options show marginal and transient benefits.[4] Among these, epidural steroid injection (ESI) is the most common interventional technique for pain management. In 2003, the total number of spinal injections performed in the United States was estimated at 12 to 15 million,[5] with the number steadily increasing between 2000 and 2014.[4] The procedure involves injecting corticosteroid and anesthetic drugs into the epidural space in order to reduce inflammation and pain.[6] Current practice guidelines advise that spinal injections be performed under fluoroscopy guidance.[7] However, because fluoroscopy is inherently a two-dimensional imaging modality, more than one view is required for three-dimensional positioning of the injection needle. Typical views include anteroposterior (AP), lateral (LAT), and oblique. Using these fluoroscopic views, the needle can be guided to the target area, and contrast can be injected under conventional or digital-subtraction cinefluoroscopy. This contrast

confirms that the medication will spread to the proper structures and that no harmful spread of injectate will occur.

There are some risks which are clearly linked to the procedure and commonly include worsened pain, headache, inaccurate needle placement, and fainting, but the added stochastic risk of radiation is more difficult to associate with a specific procedure. Past studies have evaluated radiation endpoints such as fluoroscopic time[8–14], tube current[9], effective dose estimation using an anthropomorphic male phantom[15], dose-area product[11–13], effective dose from radiation dosimetry badges (staff exposure)[16], and procedure time.[14] While these previously-studied endpoints are useful metrics, effective dose is a quantity that is more directly related to the radiation-induced excess risk of cancer and heritable effects; the International Commission on Radiation Protection (ICRP) approximates this excess detriment at 5% per Sv.[17]

To calculate effective doses, this study used a validated Monte Carlo simulation package (GEANT4) and computational human (XCAT) models to estimate the effective dose incurred during the lumbar spinal injection procedures of three patients. This study is the first to use Monte Carlo simulations to estimate radiation dose for epidural lumbar spinal injection procedures.

2.2 Methods

In Figure 1 (below), we show a flow chart depicting an overview of the simulation process. Individual patient procedures were recreated by finding the most similar XCAT phantom and setting up the proper beam simulations. The deposited energy is summed across all photon simulations (histories) and then converted to organ and effective doses.

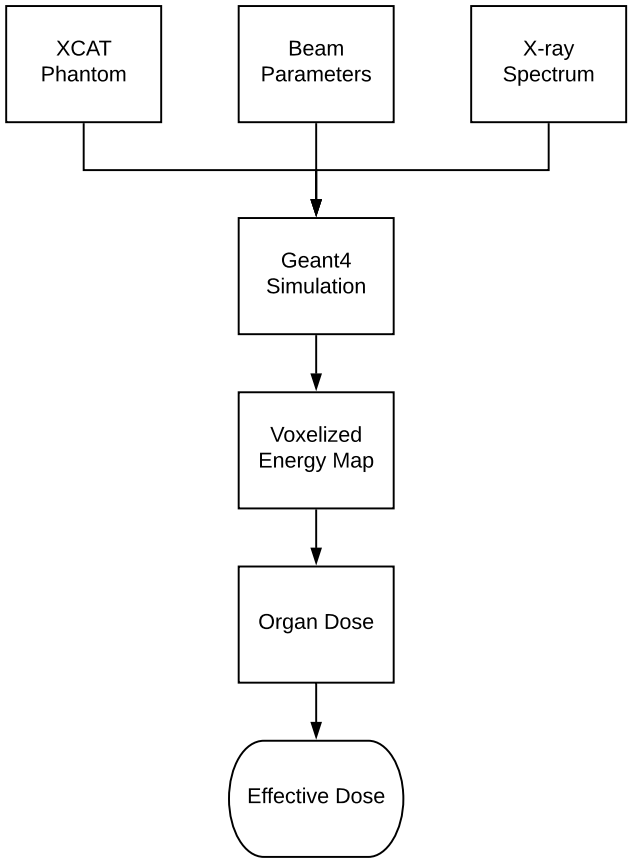

Figure 1: A flowchart outlining the overall setup and simulation process for the simulation of fluoroscopy dose and effective dose calculation

2.2.1 Patient Data

For these simulations, we used a subset of recorded data from a larger patient database. This larger data set consisted of relevant procedural and anatomical data for a study of the dose-area-product (DAP) associated with fluoroscopy-guided spinal injections. Institutional Review Board (IRB) approval and subject informed consent were obtained prior to any study-related data collection. For each patient, the study database included information on age, weight, height, body-mass-index (BMI), anteroposterior (AP) thickness, lateral thickness, procedure type, injection position, and injection side (left/right). A single, fellowship-trained, interventional spine physiatrist with six years of experience performed all injections, in accordance with the Spine Intervention Society (SIS) Guidelines.[7] All imaging was performed using a GE OEC 9900 Elite fluoroscopy system equipped with a 9'' diameter image intensifier. Each patient procedure consisted of four to six fluoroscopic imaging views, for which the database had imaging technique information: cephalocaudal arm angle, mediolateral arm angle, contrast type, cumulative time, cumulative dose, source to first surface distance (SFSD), first surface type (table bottom, table side, patient flank), signal-to-noise ratio (SNR), field area at 100 cm, field shape, kVp, and mAs. Some of these parameters were recorded at the time of the injection, while others were retrospectively calculated based on imaging data. Of the 11 types of procedures originally in the database, we limited our simulations to the

subset of transforaminal epidural steroid injections (TFESI) at the level of the 5th lumbar (L5) or 1st sacral (S1) vertebrae. The subset of data used in this study consisted of six patients: two patients in each of the low, medium, and high BMI groups. The low, medium, and high BMI groups aligned CDC definitions of underweight, healthy weight, and overweight or obese, respectively.[18] The six patients had ages of 35-82, BMIs of 23-38 kg/m^2, and unspecified genders.

2.2.2 XCAT Phantoms

To simulate the six chosen patients, we selected digital human phantoms that most closely matched the following body specifications: AP thickness, lateral thickness, BMI, and height. Since patient genders were not recorded as part of this study, we used one female phantom and one male phantom for each BMI group. The phantoms were obtained from the library of XCAT virtual phantoms, which are a library of digital human phantoms based on patient CT data, described previously.[19] Below, Tables 1-3 list the pertinent data for the six patients and their corresponding phantoms.

Table 1: Data from the low-BMI group

Parameter	Patient 1	Phantom 1	Patient 2	Phantom 2
BMI (kg/m^2)	22.6	15.9	25.6	21.9
Height (m)	1.5	1.4	1.8	1.7
AP Thickness (cm)	10.0	18.4	18.0	19.4
LAT Thickness (cm)	25.0	24.0	34.0	30.4
Voxel size (mm)	--	2.0	--	3.5
Gender	--	Female	--	Male

Table 2: Data from the medium-BMI group

Parameter	Patient 3	Phantom 3	Patient 4	Phantom 4
BMI (kg/ m^2)	29.6	28.3	28.0	27.8
Height (m)	1.8	1.8	1.7	1.7
AP Thickness (cm)	24.0	24.1	23.0	24.3
LAT Thickness (cm)	34.0	33.8	32.0	34.8
Voxel size (mm)	--	3.5	--	3.5
Gender	--	Female	--	Male

Table 3: Data from the high-BMI group

Parameter	Patient 5	Phantom 5	Patient 6	Phantom 6
BMI (kg/ m^2)	36.1	36.7	37.9	38.0
Height (m)	1.7	1.5	1.6	1.8
AP Thickness (cm)	31.0	28.3	25.0	31.2
LAT Thickness (cm)	41.0	38.0	40.0	45.2
Voxel size (mm)	--	3.5	--	3.5
Gender	--	Female	--	Male

The XCAT phantoms are natively stored as non-uniform rational basis spline (NURBS) files and were converted to voxelized binary files for GEANT4. Each phantom has two such voxelized files: one specifies the organ at each voxel and the second specifies the material composition of each voxel. Each material is assigned a specific density (Table 4); the elemental compositions can be found in the provided references. To reduce the number of materials in the simulation, all soft tissue organs used the same material definition, except for lung and breast tissue. This approximation was considered reasonable because tissue density, which is the most important parameter

affecting dose deposition, does not change by more than 4% between the soft-tissue organs.

Table 4: The density and reference for each material used in this simulation

Organ ID	Material	Density (g/cm3)	Reference
Breast	50/50 Whole Breast	0.96	ICRU report 46, Appendix A[20]
Lung	Avg. Inflated Lung	0.26	NCRP Report 46 [21]
Skeleton	Avg. Skeletal Bone	1.40	Cristy 1987, Table A-1[22]
Other Organs	Average Soft Tissue	1.03	ICRU report 46, Appendix A
Air	Air	1.205×10^{-3}	NIST
Table Inside	Acrylic Foam	0.10	Li et al. 2011[23]
Table Outside	Carbon Fiber	1.70	Li et al. 2011

The final element of the patient modeling was the addition of the table used in these procedures, which was not included or different in original XCAT phantom. The fluoroscopy table (Acroma, Model: 0047-TM3MP) is specified to contain 38.1 mm of acrylic foam and 1.3 mm of carbon fiber shell. To model this table, foam and carbon fiber were added to the anterior side of the patient, with the number of voxels matching the specified thickness as closely as the resolution of phantom file allowed (see pixel size,

Tables 1-3). The volume outside of the phantom and table was filled with voxels of air, at standard temperature and pressure.

2.2.3 Monte Carlo Beam Models

GEANT4 was chosen as the Monte Carlo simulation package for this section because it is a robust toolkit, with over two decades of development providing a "complete range of functionality including tracking, geometry, physics modeling, and hits."[24] Though originally developed for high-energy physics research, it can be used for low-energy physics processes (eV-range) and has been used for many medical imaging studies.[25–31] GEANT4 has also been used in validation studies for medical imaging, namely the AAPM Report of Task Group 195, which is intended to enable other scientists to benchmark their Monte Carlo codes.[31]

GEANT4 allows users to specify the types of physics interactions that are simulated. For these simulations, we used the "G4EmPenelopePhysics" package, which includes Compton scattering, Rayleigh scattering, gamma conversion, photoelectric effect, bremsstrahlung, ionization, and positron annihilation. To handle the large voxelized human models, GEANT4 was configured with nested parameterization. GEANT4 also allows users to specify a cutoff for secondary particles created by interactions, for which we chose an energy cutoff of 250 eV and a range cutoff of 0.1 mm. Secondary particles with energies or ranges lower than these cutoffs instead had their

energy deposited in the current voxel. The range of particles was chosen to be an order of magnitude less than the size of the voxels, so that secondary particles were only simulated if they were going to leave the voxel.

Each simulation was modeled after the corresponding patient procedure and consisted of four to six views, where each view was computed using an independent simulation in GEANT4. Each beam was modeled as a divergent cone beam with a circular field as an approximation of the octagonal X-ray field of the real procedure (see Figure 2, below).

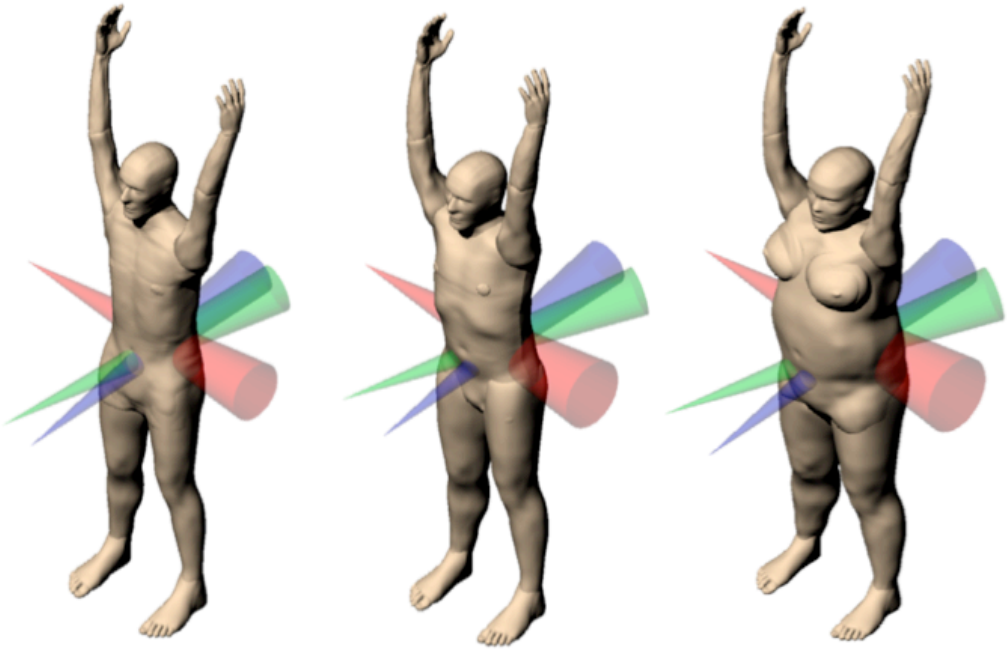

Figure 2: Beam and surface renders of the XCAT phantoms used for patients 2, 4, and 5. These renders were made before voxelization and the beams are not drawn to scale.

Each beam was configured based on kVp, mAs, injection position, beam angles, source-to-contact distance, and field size. The spectrum for each beam was created with Spektr 3.0, which uses the TASMICS model to model a tungsten anode spectrum.[32] The TASMICS model included 1.6 mm of inherent aluminum filtration and 0% voltage ripple. It should be noted that filtration can be added but not removed, and that the filtration for this fluoroscopy tube was reported as 0.6 mm Aluminum.[33] The effect on the total flux was taken into account by normalizing the results to dose area product (see section 2.2.7). To verify that the spectrum was being properly generated in GEANT4, we recorded the starting energy of 10^4 photons and confirmed that this energy distribution was the same as the input spectrum.

The beam source location was calculated using the three following steps (shown in Figure 3).

1. Find the isocenter, i.e. the location of the spinal epidural space, between the L5 and S1 vertebrae.
2. Use the fluoroscopy arm angles to determine the unit vector for the direction of the center of the beam.
3. Follow beam direction vector backwards from the isocenter to the first-surface point (either the table bottom or patient flank) and add that to the isocenter position.

4. Follow the beam direction vector backwards from the first-surface point to a distance indicated by the source-to-first-surface distance and then add this to the point determined in step (3).

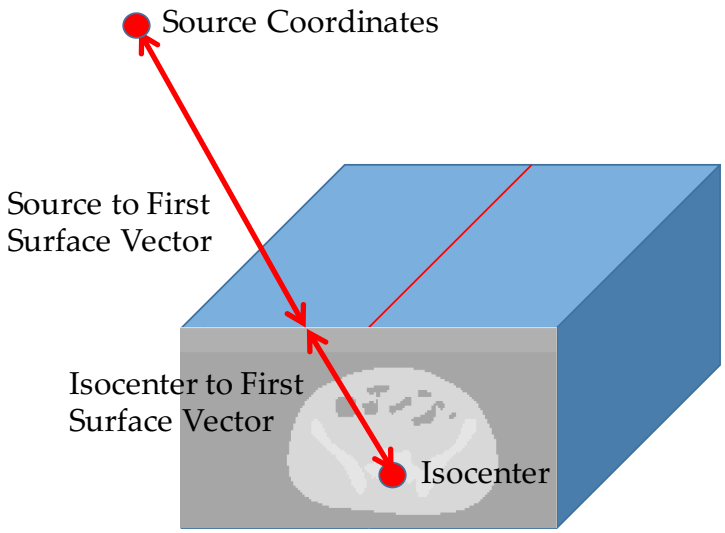

Figure 3: A depiction of how the radiation source location is determined

Next, the field area was used to determine the angular spread of the circular cone beam. For a circular field area (A), which was recorded at 100 cm from the source, the angular spread was determined with the following equation:

$$\theta = \tan\left(\frac{\sqrt{A}/\pi}{100\ cm}\right)$$

To specify the direction of the beam with GEANT4's general particle source, the user must specify two vectors "rot1" and "rot2". These vectors indicate the x' and y' vectors for the source coordinate system, respectively. Photon direction vectors were

always relative to the direction of the negative z′ vector. For example, if rot1 was specified as [0, 0, 1] and rot2 as [0, 1, 0], then photons would be emitted in the global –x direction. An illustration of this situation is shown below.

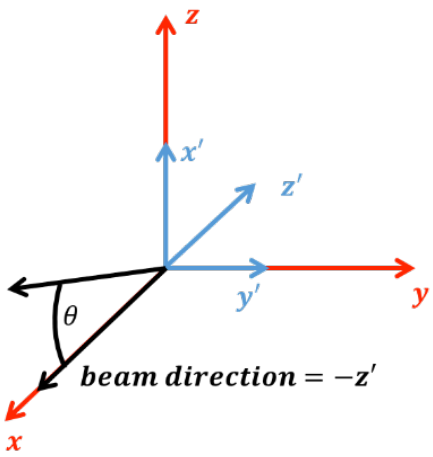

Figure 4: The transformation of coordinates used for the GEANT4 general particle source when x′ is in the z direction and y′ is in the y direction.

To transform the cephalocaudal arm angle (θ_{CC}) and mediolateral arm angle (θ_{ML}) to general particle source vectors, the following equations were derived.

$$rot1 = < \cos(\theta_{CC}) * \cos(-\theta_{ML}) , -\cos(\theta_{CC}) * \sin(-\theta_{ML}) , \sin(\theta_{CC}) * \sin(-\theta_{ML}) >$$

$$rot2 = < 0 , \sin(\theta_{CC}) , \cos(\theta_{CC}) >$$

The orientation of the beam, relative to the phantom, was visually verified through the final dose distributions and the GEANT4 graphical display. Finally, isotropic distribution of photons was checked by recording the initial momentum

vectors for 10^4 particles and verifying the output distribution against the expected distribution.

Each beam was simulated with 10^7 photons per view – this number was determined to reduce the statistical uncertainty of the whole-body effective dose (see section 2.2.5) to below 3%. GEANT4 was set up to record and sum the deposited energy from each particle. These absorbed energy results were then scaled to the proper number of photons, multiplying the deposited energy by the following factor

$$k = \frac{(photons\ per\ mAs)*mAs}{10^7\ photons}$$

The number of photons per mAs was reported by SPEKTR, and the total mAs was extracted from the patient data.

2.2.4 Model Validation

Before calculating patient doses, we first validated our GEANT4 simulation model against the simulation data from AAPM TG-195.[31] This task group report was written to serve as a reference data set for Monte Carlo code validation in medical imaging. We chose to compare our code to the simulation described in Section 3.E of TG-195, which involves the use of a voxelized human phantom and CT projections. Section 3.E was chosen as a reference because it is the most anatomically complex case and most comparable to our simulation. From the details in the report, the source was to be

positioned 60 cm away from the center of a voxelized phantom, provided by the report. The fan beam had a craniocaudal width of 10 mm and a mediolateral width of 500 mm, as measured at the center of the phantom. The beam spectrum consisted of monoenergetic 56.4 keV photons. We reproduced this setup and then compared the deposited energy per history (eV), for those organs considered in TG-195. The number of histories was set to 2×10^8, so that the total deposited energy uncertainty was less than 1%, for each organ.

2.2.5 Dose Calculation

To calculate the dose to the n^{th} voxel, the following equation was used:

$$D_n = \frac{(E_n) \cdot \left(1.60218 \cdot 10^{-16} \frac{mJ}{eV}\right)}{\rho_n \cdot L^3}$$

where D_n is the dose to the n^{th} voxel, E_n is the absorbed energy in the n^{th} voxel, ρ_n is the density of the n^{th} voxel, and L is the size of one edge of the voxels in the phantom (the voxels are cubic). The voxel sizes can be found in Tables 1-3 and the material densities can be found in Table 4. The procedure was the same when calculating whole organ dose, except that the energy and density were summed over the voxels that are part of the organ. To calculate uncertainty, each beam was simulated 100 times. The standard deviation for each organ dose was calculated as the standard deviation across the 100 trials.

2.2.6 Effective Dose Calculation

Effective doses were calculated from absorbed doses with the tissue weighting factors given by ICRP publication 103.[17] Bone marrow was not explicitly modeled in these XCAT phantoms, so it was estimated using the mass-energy attenuation coefficient method described by Lee et al. (2006).[34] In this method, the dose to the bone marrow of the k^{th} bone ($D_{RBM,k}$) is calculated from the dose to homogenous average k^{th} bone ($D_{HB,k}$) using the following equation:

$$D_{RBM,k} = D_{HB,k} \cdot \frac{\left[\frac{\mu_{en}}{\rho}(E)\right]_{RBM}}{\left[\frac{\mu_{en}}{\rho}(E)\right]_{HB}} \cdot S_k(E, age)$$

The values in the second term are the mass-energy attenuation coefficients (MEAC) for red bone marrow (on top) and homogeneous average bone (on bottom). An energy-averaged ratio of mass-energy attenuation coefficients was calculated, from the data given by Lee et al (2006):[34]

$$\overline{[MEAC(E)]_{HB}^{RBM}} = \frac{\sum_E \left\{ I(E)^* \left(\left[\frac{\mu_{en}}{\rho}(E)\right]_{RBM} \Big/ \left[\frac{\mu_{en}}{\rho}(E)\right]_{HB} \right) \right\}}{\sum_E I(E)}$$

where I(E) is the intensity of the photon spectrum at a given energy, interpolated on a logarithmic scale. S_k is a term that accounts for enhancement in the photoelectric interaction of photons with the bone surface, which thereby increases the bone marrow dose. The photoelectric enhancement depends on the energy of photons hitting the

bones, the age of patient, as well as the bone in question (k). The values used in this study were taken from experimental measurements by King and Spiers (1985),[35] which are still considered the most detailed available.[34] Because these values were only measured for three age groups (20 months, 9 years and 44 years), we chose the closest age to the fluoroscopy patients (44 years old). For bones not explicitly given in this paper, we used the average skeletal bone data. Because our photons are not monoenergetic, the average energy of the photon spectrum was used for S_k:

$$\bar{E} = \frac{\sum_E I(E)*E}{\sum_E I(E)}$$

Thus, the final equation for the marrow dose in the k^{th} bone was

$$D_{RBM,k} = D_{HB,k} \cdot \overline{[MEAC(E)]}_{HB}^{RBM} \cdot S_k(\bar{E}, age)$$

where MEAC and $S_k(E)$ values were determined via linear interpolation.

Values of red bone marrow dose were calculated for each bone, and then summed together as a weighted fraction of each bone's contribution to the total mass of marrow in the body ($f_{RBM,k}$), for the k^{th} bone. These fractions were derived from Cristy (1981).[36] The resulting equation for effective dose contribution from bone marrow was

$$ED_{RBM} = \sum_{k \,\epsilon\, bones} f_{RBM,k} \cdot D_{RBM,k}$$

For the effective dose contribution from bone surface, the average dose across all the bones was used. This is a common approach to use, when bone microstructure data is not available.[34]

When experimentally determining effective dose, absorbed doses are typically measured at points within the field.[37] Thus, for distributed organs such as the skin, bone surfaces, and bone marrow, values would only be comparable if doses were calculated with voxels within the beam. Thus, for skin, bone surface, and marrow, we excluded dose voxels outside of the primary beam. Standard deviation values were carried through the effective dose calculation, when the organ doses were multiplied by radiation weighting factors.

2.2.7 Dose Area Product Normalization

To make the effective dose results comparable to other systems, the effective doses were normalized to a Monte-Carlo simulated dose area product (DAP). This also helped to correct for the magnitude of fluence in our simulation, which was likely lower than the actual x-ray tube flux, due to the increased filtration. To calculate DAP, GEANT4 was set up with a scoring volume at 100 cm from the source. The scoring volume was an air-filled disk, 2 cm in thickness and 6 cm in diameter. The diameter was chosen such that the disk would fit fully within any of the beams, at a distance of 100 cm. Using the same beam definitions as the fluoroscopy simulations, the irradiations

were simulated with $5x10^8$ photons per beam. This number of histories was chosen so that the statistical uncertainty in dose would be less than 1%. This dose was then multiplied by the area of the field, which was scaled from the recorded distance (28 cm to 41 cm) to 100 cm, by the square of the distance. The entire simulation was performed in air.

2.3 Results

2.3.1 Model Validation

In this section, we show the results of the comparison between our GEANT4 simulation and the monoenergetic GEANT4 simulation data from section 3.E of TG-195. These results are only shown for organs whose absorbed energy is reported in TG 195. Approximately 90% of our organ dose estimates were within 4% of TG-195, with our results being lower than those of TG-195, on average.

Table 5: Dose results from monoenergetic CT projections

Organ	Absorbed Energy per Projection Angle (keV)							
	0°	45°	90°	135°	180°	225°	270°	315°
Soft tissue	11.57	11.70	9.85	9.56	9.71	9.46	9.84	11.62
Heart	3.04	1.91	0.77	0.75	1.24	1.19	1.60	2.68
Lung	1.29	1.03	0.67	0.74	1.07	0.71	0.62	0.91
Liver	0.67	0.67	0.48	0.41	0.40	0.25	0.16	0.40
Gallbladder	6.37×10^{-3}	6.33×10^{-3}	3.94×10^{-3}	2.62×10^{-3}	2.52×10^{-3}	1.52×10^{-3}	1.25×10^{-3}	3.99×10^{-3}
Spleen	1.74×10^{-2}	9.76×10^{-3}	6.06×10^{-3}	1.78×10^{-2}	3.31×10^{-2}	3.65×10^{-2}	3.26×10^{-2}	2.60×10^{-2}
Stomach	0.13	8.16×10^{-2}	3.51×10^{-2}	5.68×10^{-2}	0.11	0.12	0.13	0.15
Large Intestine	1.64×10^{-2}	9.09×10^{-3}	3.00×10^{-3}	4.95×10^{-3}	9.93×10^{-3}	1.18×10^{-2}	1.74×10^{-2}	2.01×10^{-2}
Pancreas	8.53×10^{-3}	6.02×10^{-3}	3.07×10^{-3}	4.36×10^{-3}	7.00×10^{-3}	7.13×10^{-3}	7.50×10^{-3}	8.94×10^{-3}
Adrenal	1.50×10^{-4}	1.30×10^{-4}	1.00×10^{-4}	1.40×10^{-4}	1.80×10^{-4}	1.60×10^{-4}	1.10×10^{-4}	1.40×10^{-4}
Thyroid	1.70×10^{-3}	1.38×10^{-3}	1.02×10^{-3}	1.25×10^{-3}	1.54×10^{-3}	1.32×10^{-3}	1.21×10^{-3}	1.52×10^{-3}
Thymus	4.37×10^{-2}	3.60×10^{-2}	1.66×10^{-2}	1.20×10^{-2}	1.10×10^{-2}	8.87×10^{-3}	1.11×10^{-2}	2.86×10^{-2}
Small Intestine	1.05×10^{-2}	7.49×10^{-3}	3.23×10^{-3}	3.53×10^{-3}	5.41×10^{-3}	5.37×10^{-3}	7.08×10^{-3}	1.02×10^{-2}
Esophagus	3.64×10^{-2}	3.27×10^{-2}	2.25×10^{-2}	2.57×10^{-2}	3.14×10^{-2}	3.09×10^{-2}	2.39×10^{-2}	2.98×10^{-2}
Skin	0.46	0.44	0.28	0.19	0.13	0.20	0.30	0.46
Breast	2.14×10^{-2}	1.76×10^{-2}	6.70×10^{-3}	2.06×10^{-3}	2.78×10^{-3}	1.98×10^{-3}	7.05×10^{-3}	1.80×10^{-2}
Cortical Bone	8.74	7.63	5.55	8.48	10.98	8.34	5.82	7.38

Table 6: Original reference dose values from TG-195 for the monoenergetic chest CT projections using GEANT4

Organ	Absorbed Energy per Projection Angle (keV)							
	0°	45°	90°	135°	180°	225°	270°	315°
Soft tissue	11.57	11.76	9.98	9.58	9.70	9.49	9.97	11.65
Heart	3.09	1.93	0.79	0.77	1.27	1.20	1.63	2.73
Lung	1.30	1.05	0.68	0.76	1.09	0.72	0.64	0.92
Liver	0.68	0.68	0.50	0.42	0.41	0.25	0.17	0.41
Gallbladder	6.37×10^{-3}	6.33×10^{-3}	3.94×10^{-3}	2.62×10^{-3}	2.52×10^{-3}	1.52×10^{-3}	1.25×10^{-3}	3.99×10^{-3}
Spleen	1.76×10^{-2}	9.91×10^{-3}	6.27×10^{-3}	1.81×10^{-2}	3.38×10^{-2}	3.74×10^{-2}	3.34×10^{-2}	2.65×10^{-2}
Stomach	0.13	8.30×10^{-2}	3.62×10^{-2}	5.81×10^{-2}	0.11	0.12	0.14	0.16
Large Intestine	1.67×10^{-2}	9.22×10^{-3}	3.15×10^{-3}	5.07×10^{-3}	1.02×10^{-2}	1.20×10^{-2}	1.79×10^{-2}	2.07×10^{-2}
Pancreas	8.79×10^{-3}	6.18×10^{-3}	3.15×10^{-3}	4.38×10^{-3}	7.15×10^{-3}	7.31×10^{-3}	7.68×10^{-3}	9.13×10^{-3}
Adrenal	1.50×10^{-4}	1.30×10^{-4}	1.00×10^{-4}	1.50×10^{-4}	1.80×10^{-4}	1.60×10^{-4}	1.20×10^{-4}	1.30×10^{-4}
Thyroid	1.74×10^{-3}	1.47×10^{-3}	1.06×10^{-3}	1.27×10^{-3}	1.57×10^{-3}	1.38×10^{-3}	1.26×10^{-3}	1.55×10^{-3}
Thymus	4.42×10^{-2}	3.64×10^{-2}	1.69×10^{-2}	1.20×10^{-2}	1.12×10^{-2}	8.95×10^{-3}	1.13×10^{-2}	2.89×10^{-2}
Small Intestine	1.07×10^{-2}	7.64×10^{-3}	3.38×10^{-3}	3.61×10^{-3}	5.51×10^{-3}	5.48×10^{-3}	7.29×10^{-3}	1.05×10^{-2}
Esophagus	3.69×10^{-2}	3.35×10^{-2}	2.30×10^{-2}	2.64×10^{-2}	3.21×10^{-2}	3.15×10^{-2}	2.44×10^{-2}	3.04×10^{-2}
Skin	0.46	0.44	0.29	0.19	0.13	0.20	0.30	0.46
Breast	2.17×10^{-2}	1.80×10^{-2}	6.80×10^{-3}	2.07×10^{-3}	2.82×10^{-3}	2.00×10^{-3}	7.18×10^{-3}	1.84×10^{-2}
Cortical Bone	8.76	7.67	5.61	8.51	11.00	8.37	5.88	7.39

Table 7: The percent difference between the validation results of this project and the original data supplied by TG-195 for a monoenergetic chest CT projections

Organ	Absorbed Energy per Projection Angle (keV)							
	0°	45°	90°	135°	180°	225°	270°	315°
Soft tissue	-0.05	-0.56	-1.29	-0.26	0.10	-0.26	-1.28	-0.21
Heart	-1.41	-1.31	-1.77	-1.44	-1.60	-1.31	-1.72	-1.49
Lung	-1.01	-1.52	-1.70	-1.43	-1.37	-1.37	-1.84	-0.97
Liver	-1.90	-2.28	-2.25	-2.09	-1.85	-1.82	-2.49	-1.47
Gallbladder	-3.05	-3.35	-4.36	-2.77	-3.46	-2.86	-5.80	-1.26
Spleen	-1.12	-1.57	-3.49	-1.48	-1.91	-2.38	-2.47	-1.95
Stomach	-1.91	-1.69	-2.98	-2.12	-1.70	-2.01	-2.47	-1.98
Large Intestine	-2.07	-1.48	-4.72	-2.35	-2.48	-1.81	-3.01	-2.83
Pancreas	-3.02	-2.69	-2.39	-0.54	-2.17	-2.48	-2.29	-2.10
Adrenal	-1.81	-0.53	-4.26	-5.10	-3.47	0.43	-7.44	7.76
Thyroid	-2.42	-6.00	-3.14	-1.36	-1.35	-4.07	-4.16	-2.12
Thymus	-1.19	-0.98	-1.68	-0.66	-1.80	-0.89	-1.20	-1.05
Small Intestine	-2.10	-2.08	-4.30	-2.42	-1.81	-2.16	-2.88	-2.42
Esophagus	-1.32	-2.24	-2.21	-2.48	-2.12	-2.01	-1.86	-1.99
Skin	0.43	-0.28	-1.05	0.50	0.41	0.85	-0.93	0.06
Breast	-1.40	-1.99	-1.34	-0.58	-1.30	-0.98	-1.88	-1.96
Cortical Bone	-0.24	-0.45	-1.11	-0.37	-0.18	-0.36	-1.00	-0.15

2.3.2 Effective Dose Results

Next, the DAP-normalized effective dose results (or dose conversion coefficients, DCCE) are shown for each patient – calculated for each beam and then for the sum of beams for the patient. The effective dose values for a given procedure ranged from 0.25 mSv[Gy cm^2]$^{-1}$ to 0.49 mSv[Gy cm^2]$^{-1}$, with an average effective dose of 0.32 mSv[Gy cm^2]$^{-1}$. Individual views had DCCE values of between 0.20 and 0.59 mSv[Gy cm^2]$^{-1}$, with an average of 0.36 mSv[Gy cm^2]$^{-1}$. The uncertainties of effective dose and DCCE values were below 4% for all simulated beams.

Table 8: Effective dose simulation results, grouped by fluoroscopic view and patient

Patient	View	Beam Area at 100 cm SID (cm^2)	kVp	Simulated DAP (Gy cm^2)	Dose Conversion Coefficient per View (mSv[Gy cm^2]$^{-1}$)	Total Dose Conversion Coefficient (mSv[Gy cm^2]$^{-1}$)
Patient 1: Low BMI Female	Oblique	178.6	85	0.15	0.55	0.49
	AP	230.2	84	0.36	0.59	
	Lateral	229.3	113	0.02	0.51	
	Lateral	229.3	111	1.99	0.47	
	Contrast (AP)	268.3	79	0.26	0.56	
	Contrast (AP)	263.4	79	2.65	0.48	
Patient 2: Low BMI Male	Oblique	182.5	100	0.24	0.36	0.33
	AP	270.0	96	0.22	0.51	
	Lateral	269.3	118	0.12	0.32	
	Contrast (AP)	305.0	92	1.91	0.30	
Patient 3: Mid BMI Female	Oblique	211.9	106	0.28	0.33	0.31
	AP	263.0	104	0.66	0.34	
	Lateral	263.6	119	0.10	0.31	
	Contrast (AP)	290.3	100	1.29	0.29	
Patient 4: Mid BMI Male	Oblique	232.9	104	0.46	0.34	0.26
	AP	232.6	100	0.16	0.31	
	Lateral	415.5	120	0.44	0.29	
	Contrast (AP)	337.1	92	1.65	0.22	
Patient 5: High BMI Female	Oblique	221.7	113	0.72	0.34	0.28
	AP	220.6	111	0.36	0.35	
	Lateral	415.5	120	0.78	0.24	
	Contrast (AP)	320.0	104	4.64	0.27	
Patient 6: High BMI Male	Oblique	283.6	113	1.05	0.28	0.24
	AP	282.1	110	0.29	0.25	
	Lateral	415.5	120	0.88	0.20	
	Contrast (AP)	311.8	108	0.97	0.23	

Figure 5 (below) shows the DCCE values for each view, grouped by the type of view (AP, Lateral, Contrast, Oblique).

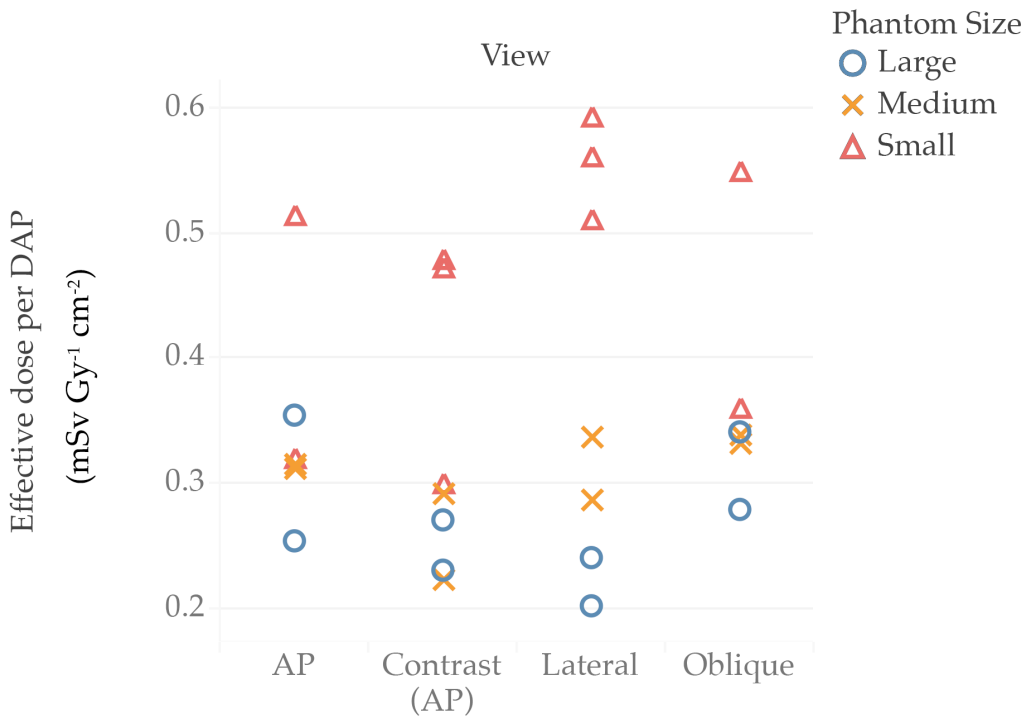

Figure 5: Effective dose results normalized to DAP, for each view. Colors correspond to different BMI groups.

2.4 Discussion

These results are both reasonable and expected given the variation in DAP and variability in size of the patients. For comparison, a similar study by Hoang et al. studied the fluoroscopic dose in spinal injection procedures with an anthropomorphic phantom and measured effective dose per kerma area product (KAP) to be 0.33 mSv Gy^{-1} cm^{-2}.[37] For quantities measured in air, DAP and KAP are considered interchangeable

terms for the same quantity[38] This is very similar to our average effective whole-body dose of 0.32 mSv[Gy cm^2]$^{-1}$ per procedure, and overlaps with our statistical uncertainty. If we use machine reported DAP values to scale the DCCE value for each beam, we calculated an average effective dose of 0.51 mSv per procedure. However, there is an important distinction to make between spinal injection procedures and other diagnostic imaging procedures; spinal injection procedures can be performed several times a year. A previous study reported an average of 4.46 ± 6.44 spinal injections performed per year, with a median of 2 and a range of 2-152 (152 is most likely an outlier).[39] Based on our average effective dose, if an individual were to receive 6 such spinal injections, the total effective dose would be 3.1 mSv, which is equal to the effective dose from a cardiac angiography (3.1 mSv), as reported by Leung et al. (1996)[40] and Vilar-Palop et al. (2016)[41]. However, this comparison does not consider the radiobiological differences of receiving the dose at one time, versus spread over an extended time, which are still uncertain at the time of this study.

Looking at the dose area product of each view (Table 9), it was apparent that the largest contribution in dose came from the AP contrast scans. Patient 1 (the low-BMI female) had the highest dose, which was expected, given that it had the most beams of any of the patients and the highest cumulative DAP. When we considered DCCE values for individual images, we found that these values were more clustered and fell in the

range of 0.20 – 0.59 mSv[Gy cm^2]$^{-1}$. There was no clear trend where certain types of views had the highest DCCE values.

The data of these simulations (Figure 4) suggested that the DCCE increased as patient size decreased, though more simulations are needed to confirm this trend. In addition, the stochastic effects of radiation dose are more likely to manifest in younger patients, who also tend to be smaller. Thus, the overall conclusion is that dose is an especially important consideration for younger and smaller patients, if they would receive many such injections under image guidance.

There are several limitations to the simulations performed in this study. First, machine data was only automatically collected for the exposures that were associated with a saved image. If any images were unrecorded, then our simulations would have underestimated the doses. Second, the accuracy of the simulations may also be reduced by the fact that the phantoms did not exactly match the patients (in terms of AP thickness, lateral thickness, and BMI). Finally, the number of patient procedures is small. There are plans for future studies to improve the efficiency of the workflow and simulate a larger group of patient procedures.

2.5 Conclusion

The simulations provide information about the typical effective doses across a range of patients and beam orientations for spinal injection procedures. The

characteristics and magnitude of the dose data will help to inform the clinical choices of practitioners, though the specifics will vary between clinics, patients, and physicians. For the procedures simulated in this study, the patient size did not have a dominating effect on the total patient effective dose. Rather the total DAP was a more important factor. Further, we saw that the largest contribution to the total effective dose came from the AP contrast views. However, when effective dose was normalized to DAP, we saw that the DCCE increased as BMI decreased. Thus, for patients receiving spinal injections over many years, the fluoroscopic radiation dose could be an important factor, especially for young and/or small patients. Further study of effective dose variability and the associated risk is warranted, so that we may better understand the risk-benefit ratio for patients considering on-going spinal injections for pain management.

3 The Effect of Patient Size on Organ Dose Homogeneity

3.1 Introduction

Previous work by Samei et al. estimated the dose heterogeneity for chest CT procedures, using a single male phantom and the PENELOPE Monte Carlo toolkit.[42] The goal of this portion of the thesis was to expand and study heterogeneity calculations for a larger group of patients – essentially conducting a virtual clinical trial. With the advent of more efficient, GPU-accelerated Monte Carlo simulation codes, it is now feasible to perform these simulations on a larger number of phantoms and with a larger number of histories. It is important to study organ-dose volume heterogeneity for differently-sized patients and different protocols because the heterogeneity may be affected by body size as well as the protocol used. In cases with considerable dose heterogeneity, the calculation method may especially affect the effective dose results. In previous simulations of effective dose in CT, the mean organ doses were used in the effective dose calculations for all organs except the skin and bones. For the skin and bones, the dose was only considered for those regions of the patient that were directly within the beam.[23] This makes sense when comparing to experimental measurements, because the dosimeters are typically placed within the beam. However, this raises the question of how to most accurately calculate absorbed dose and effective dose. In this study, we investigated the change in absorbed dose when the calculation is performed using only

voxels within the beam versus using all the voxels. Further, we examined the effect of these different calculations on the absorbed and tissue-weighted dose quantities. We also performed these simulations and calculations across a large range of patients, so that the results could be more representative and robust with respect to patient variation.

Because of the number of simulations and voxels required, a GPU-accelerated Monte Carlo simulation package (MCGPU) was used for this portion of the work.[43] MCGPU was chosen because it is up to 27 times faster than traditional Monte Carlo packages[43], allows for voxelized phantom input and voxelized dose output, and was specifically designed for CT simulations. MCGPU CT simulations have been recently validated against experimentally verified PENELOPE simulations and against simulations from section 3.E of TG-195 (TG-195 is described in section 2.2.4).[44] At the time of this work, MCGPU can be freely downloaded from the internet.

3.2 Methods

3.2.1 XCAT Phantoms

As in the previous section, voxelized XCAT phantoms were used to model human patients. For each material used in an MCGPU simulation, an input file is required. Each file contains the density, mean free paths for each type of interaction, Rayleigh scattering form factors, and Compton interaction profiles. The mean free paths,

form factors, and interaction profiles were previously generated using Monte Carlo simulations in PENELOPE 2006 and are included with the MCGPU toolkit. The materials used in this simulation were the same as the previous simulation, except the air, table foam, and table shell. The air, bed foam interior, and bed outer shell were not included in this simulation, as these materials slow the simulation down and do not noticeably change the simulation results.

3.2.2 MCGPU Simulation

Next, we discuss the methods used to simulate the helical CT scans of a multidetector array CT scanner (Lightspeed VCT, GE Healthcare, Waukesha, WI). In this study, we focused on chest and abdominopelvic scan protocols. These protocols were chosen because they are two of the most common types of CT scans,[45] and cover regions of density inhomogeneity: the low-density region in the lungs and the high-density structures of the pelvis. Of the other common CT scan types, spine and trunk exams contain similar areas of the body, while neck, head, and extremity scans typically have lower effective dose values.[41]

Specifically, we chose to replicate the chest and abdominopelvic scan parameters presented by Tian et al.[46] The chest scans covered the entire length of the lung, which resulted in scan lengths from 17.7 to 39.5 cm, with an average of 28.2 cm. The abdominopelvic scans covered the area of the body from the top of the liver to 1 cm

below the ischium, which resulted in scan lengths of 20.8 to 58.8 cm, with an average of 36.9 cm. These scan lengths included 3.2 cm of extra scanning on both ends (overranging), in accordance with the GE adult and pediatric body protocols reported by Tian et al.[46] and Li et al.,[23] respectively. Following the same protocols, all scans used a 120 kVp spectrum, a pitch of 1.375, 4.48-degree collimation width, and a source to rotational axis distance of 54.1 cm. The mediolateral width of each projection was set to cover the entire width of the phantom, with projections simulated every 10 degrees. Again following the protocols referenced above, pediatric scans used a small bowtie filter and the adult scans used a medium bowtie filter. To compute the effect of the bowtie filters, we obtained a *pre-bowtie* spectrum from the vendor and applied polyenergetic Beer-Lambert attenuation. The filter was modeled with sections of graphite and aluminum, where dimensions were also provided by the vendor (see Figures 6 & 7, below).

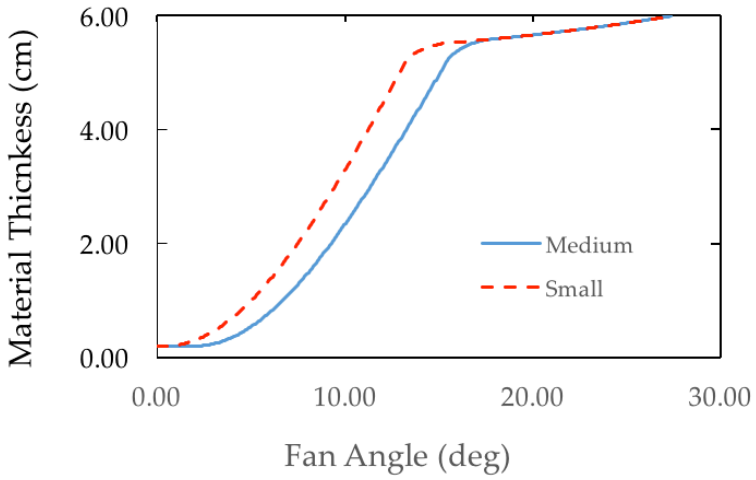

Figure 6: Graphite thickness of small and medium bowtie filters used in this study as a function of the CT fan angle

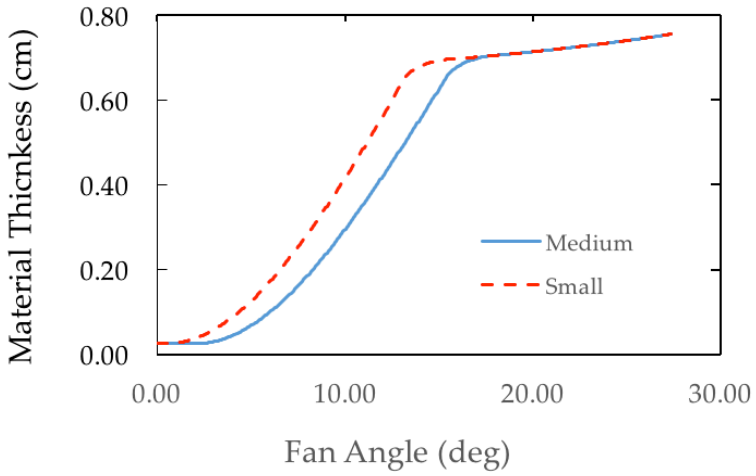

Figure 7: Aluminum thickness of small and medium bowtie filters used in this study as a function of the CT fan angle

Using standard mass attenuation coefficients (available on the NIST website) and densities, we computed the output spectrum and relative intensity reduction at each angle (see Figure 8, below). Mass attenuation coefficients were only given for some

energy values, and to calculate the values in between we used a series of piecewise cubic spline fits. 109 cubic splines were fitted for aluminum and 87 cubic splines were fitted for graphite, and mass attenuation values were calculated with these splines. Note that the output was symmetric about the central ray, the input spectrum was the same for each angle, and that no scattering processes were considered.

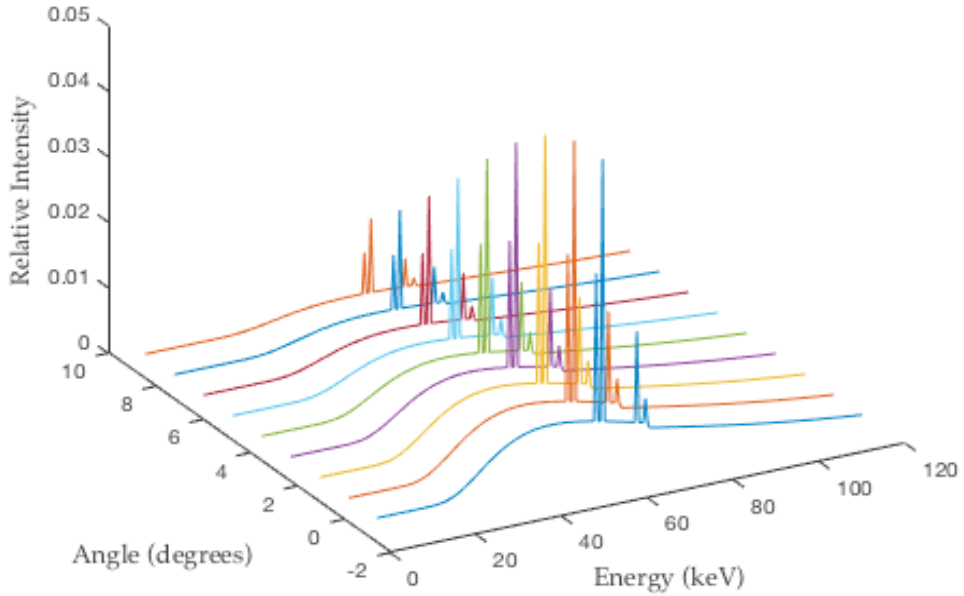

Figure 8: Post-bowtie beam spectra, as a function of fan angle (0 degrees is the central ray) for the small bowtie filter. Note that the angular distribution of the spectrum is symmetric about 0 degrees.

The simulations were performed without tube current modulation (TCM). TCM attempts to increase or decrease the number of photons in response to local variation of beam attenuation, to obtain constant image quality.[47] Thus, we expect that an image without TCM should exhibit more heterogeneity and is of more interest to this study.

3.2.3 Absorbed Dose Calculation

Dose was calculated in the same manner as the fluoroscopy simulations (see Section 2.2.5), except that dose was additionally normalized to a constant tube output of 100 mAs per rotation. The equation used to calculate dose to the nth voxel was

$$D_n = \frac{(E_n) \cdot \left(1.60218 \cdot 10^{-16} \frac{mJ}{eV}\right)}{\rho_n \cdot L^3} \cdot \frac{N_{\frac{photons}{mAs}}}{N_{hist}} \cdot 100mAs \cdot n_{rotations} \cdot OCF$$

Where E_n is the total absorbed energy in the nth voxel, ρ_n is the density of the nth voxel, L is the size of each voxel, $N_{photons/mAs}$ is the number of photons per mAs for the manufacturer-provided spectrum, N_{hist} is the number of total photons in the simulation, $n_{rotations}$ is the number of rotations for the given CT scan, and OCF is an experimentally-measured output correction factor. This correction factor was measured by Li et al. when comparing measurements to simulations of CT scans with different kVp settings.[23] Our simulations used an OCF of 1.196, which was the value determined for a 120 kVp scan. The number of rotations was calculated as the total table travel divided by the travel per rotation. Dose uncertainty was reported by MCGPU and was internally calculated through the following rearrangement of the typical standard deviation formula:

$$\sigma_n = \sqrt{\frac{1}{10^7}\sum_{i=1}^{10^7}\left(E_{i,n}\text{-}\bar{E}_n\right)^2}$$

$$\sigma_n = \sqrt{\frac{1}{10^7}\sum_{i=1}^{10^7}\left({E_{i,n}}^2\text{-}2E_{i,n}\bar{E}_n + {\bar{E}_n}^2\right)}$$

$$\sigma_n = \sqrt{\frac{1}{10^7}\left[\left(\sum_{i=1}^{10^7}{E_{i,n}}^2\right)\text{-}2(10^7\cdot\bar{E}_n)\bar{E}_n + 10^7\cdot{\bar{E}_n}^2\right]}$$

$$\sigma_n = \sqrt{\frac{1}{10^7}\left[\left(\sum_{i=1}^{10^7}{E_{i,n}}^2\right)\text{-}\frac{1}{10^7}\left(\sum_{i=1}^{10^7}E_{i,n}\right)^2\right]}$$

In this form, the term in the first pair of parentheses is the sum of squared energy depositions across all histories and the second term is the sum of energy depositions across all histories. Both quantities were recorded by MCCPU and then used to calculate the uncertainty. For the deposited energy of an organ, the terms in the parentheses are also summed over n, the voxels in the organ of interest. To convert energy uncertainty to dose uncertainty, one can simply use the energy to dose equation, given at the beginning of this section. Bone marrow dose is calculated in the same manner as described in Section 2.2.6.

3.2.4 Dose Heterogeneity

In this study, we used a set of 58 adult and 56 pediatric whole-body phantoms, which included patients with AP sizes of 11.0 to 33.8 cm, lateral sizes of 16.2 to 45.5 cm,

and effective diameters of 13.8 to 37.9 cm. Lateral and AP thickness values were extracted from the phantoms by finding the anterior, posterior, left, and right edges of the chest, at the level of the base of the lung. Effective diameters were calculated as the geometric mean of the AP and lateral dimensions (see below), per the report of AAPM Task Group 204.[48]

$$Effective\ diameter = \sqrt{AP \cdot LAT}$$

The distribution of effective diameters, across all the patients, is shown below.

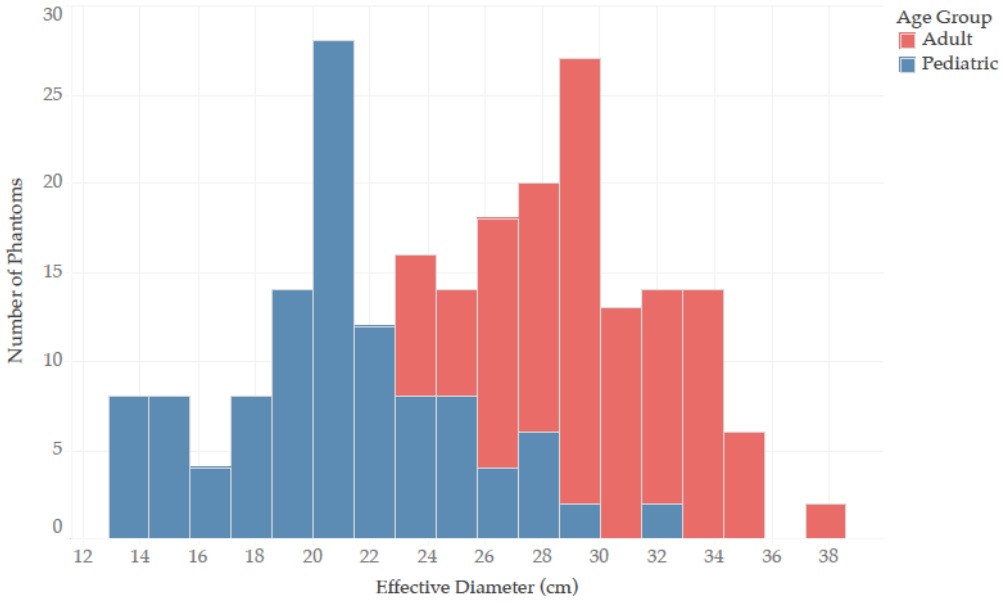

Figure 9: The distribution of effective diameters, for adult and pediatric phantoms included in this study.

BMI values were not included in the final analysis because the pediatric phantoms did not include arms and this would skew any comparison between the groups. There are certainly other ways to calculate effective diameter as described in TG-204,[48] but this geometric approach was identified as the most reasonable implementation.

In addition to effective diameter, we also investigated the effect of organ depth as a function of dose heterogeneity. To calculate this metric, we first calculated the mass-weighted centroid of each slice. Then, for each organ, we calculated the average distance of voxels from the centroid positions of the corresponding slice. We expected that dose heterogeneity may change as a function of either effective diameter or average organ distance from the center.

For each dose result, we compared the organ doses and dose-volume heterogeneity characteristics. For dose-volume heterogeneity, we first considered the ratio of the 95th percentile dose voxel, to the mean dose voxel. From here on, we will refer to this ratio as R95. The 95th percentile dose was used instead of the maximum dose because the maximum dose was less robust to outliers.

3.2.5 Effect of Scan Parameters

In the context of variation of dose across organ volumes, we wanted to test the effect of pitch and number of projections per rotation on the dose results. It possible that the effects of heterogeneity are significantly influenced by the choice of these

parameters. To test the effects of pitch on organ dose and heterogeneity we repeated a series of adult abdominopelvic CT scans at a pitch of 0.6 instead of 1.375. We also simulated CT scans with 36 projections per rotation and 180 projections per rotation. We considered the absorbed dose to organs, R95, and dose-volume histograms (DVH) for each organ. DVH curves show the relative fraction of an organ that receives a given dose level, and are typically used in radiation therapy to assess dose-volume constraints.[49]

3.2.6 Tissue Weighted Dose Models

To investigate the potential impact of dose calculation models on tissue weighted dose models, we first calculated effective doses using the standard method described in ICRP 103.[17] In this method, we calculated the absorbed dose from each organ (described in Section 3.2.3) and then weighted each organ dose with the ICRP 103 tissue weighting factors. For bone surface, bone marrow, and skin dose calculations, we used only the dose contribution from voxels within the limits of the scan, as is typically done.[46,50–52]

Next, we calculated a similar dose quantity, what we called an equivalent in-field dose (EID). For this quantity, we used the same tissue weighting factors as for effective dose, but instead only considered those voxels that are within the scan limits. Organs fully outside of the scan limits did not contribute to this quantity. We then calculated an equivalent full-field dose (EFD), where we used all the voxels of each organ, including

the skin and bones and applied the same effective dose tissue weighting factors. Finally, we calculated 5 equivalent quintile doses (EDQ_1, EDQ_2,…EDQ_5). For these EDQ values, we first calculated five different dose levels for each organ (k): a dose level based on the lowest 20% of dose voxels ($D_{1,k}$), a dose level based on the next 20% of dose voxels ($D_{2,k}$), and so on. Then, for each dose level of each organ ($D_{i,k}$), we calculated the EDQ_i based on the following equation:

$$EQD_i = \sum_k w_k D_{i,k}$$

where w_k is the tissue weighting factor, again from ICRP 103.[17] This calculation resulted in 5 EDQ levels, which were calculated to estimate the spread of effective dose calculations based on different points of dose measurement. Finally, we compared the results of the calculation of these different tissue-weighted equivalent dose models: standard effective dose (ED), equivalent in-field dose (IFD), equivalent full-field dose (EFD), and equivalent quintile dose (EDQ). For all 4 of these quantities, we included a radiation quality weighting factor was, which was 1 for photons.[17]

3.3 Results

3.3.1 Dose Results

First, we present the absorbed dose results, normalized to a tube output of 100 mAs per rotation. On the next page, images of anteroposterior maximum intensity projections (MIP) of organ dose are shown for a selection of organs. The plotted organ-

scan combinations include: (a) ribs – chest, (b) thoracic vertebrae – chest, (c) pelvis – abdominopelvic, (d) liver – ambdominopelvic, (e) lumbar vertebrae – ambdominopelvic, and (f) sacrum - abdominopelvic. These plots were all extracted from the dose results of a single pediatric phantom, which had an effective diameter of 28.31 cm.

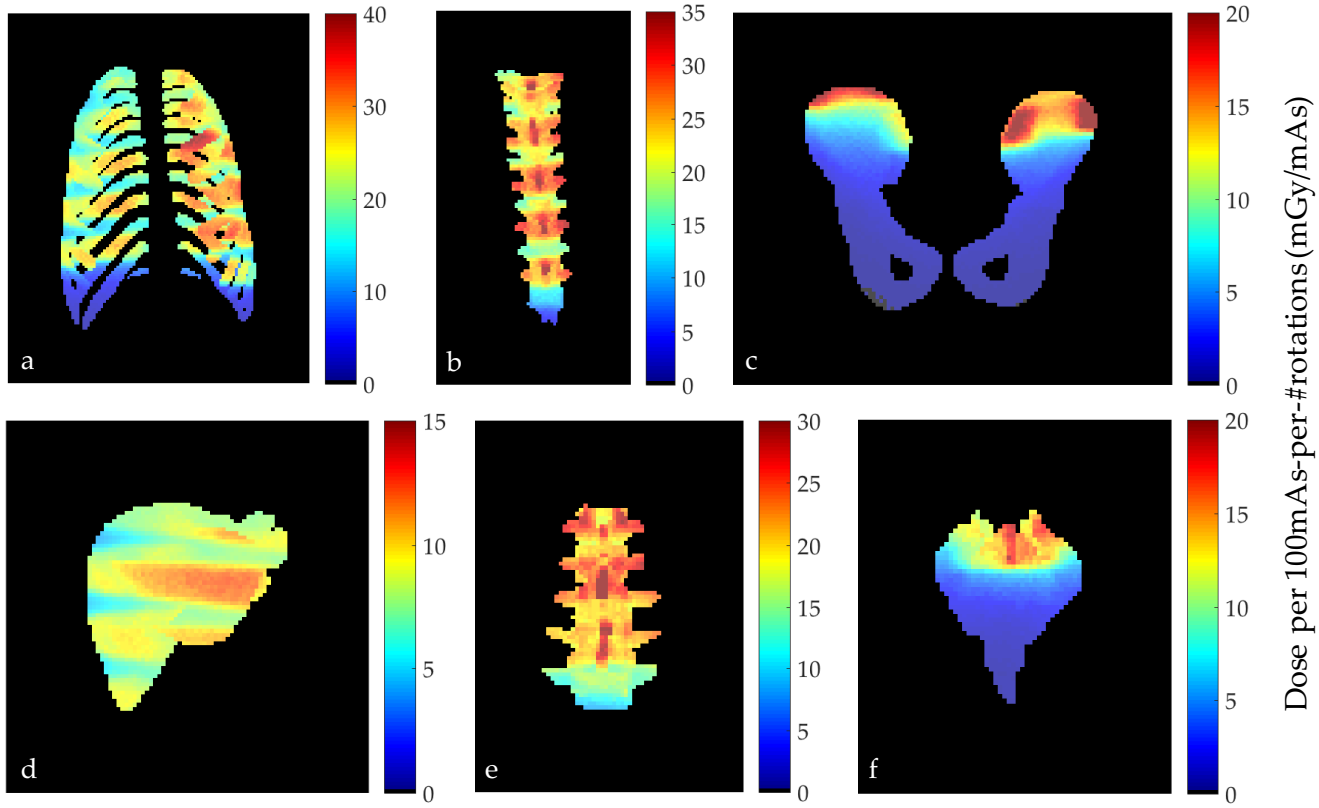

Figure 10: Anteroposterior maximum intensity projections of absorbed dose for a selection of organs: (a) ribs – chest, (b) thoracic vertebrae – chest, (c) pelvis – abdominopelvic, (d) liver – ambdominopelvic, (e) lumbar vertebrae – ambdominopelvic, and (f) sacrum - abdominopelvic. Results were normalized to a constant tube output of 100 mAs per rotation.

3.3.2 Dose Heterogeneity Results

To assess intra-organ dose heterogeneity, we calculated the 95th percentile dose divided by the mean dose for each organ (R95). In Tables 9-12, we list the minimum, average, and maximum R95 of each organ, across the 58 adult phantoms and 56 pediatric phantoms. Chest and abdominopelvic protocol simulation results have been separated into two tables. In both tables, we have separated the organs into four categories: organs completely inside the range of the CT scan, organs partially in the range of the CT scan, organs outside of the range of the CT scan, and distributed organs. Organs with asterisks (*) are only present in patients of the appropriate gender. For comparison, the adult chest protocol includes the results of Samei et al.[42], though these results are the ratio of maximum to mean dose. Bones were individually segmented and analyzed, but grouped together for the purposes of these tables.

Table 9: Ratios of 95th percentile dose to mean dose per organ, for adult chest CT scan simulations on 58 adult XCAT phantoms

Organ/structure	Min	Average	Max	Samei et al.[42]
Organs completely within CT scan range				
Breast*	1.16	1.53	2.19	--
Esophagus	1.10	1.18	1.33	1.3
Heart	1.15	1.21	1.27	1.5
Lung	1.23	1.34	1.51	1.7
Thymus	1.10	1.16	1.30	1.3
Organs partially within CT scan range				
Adrenals	1.19	1.38	1.78	1.4
Large Intestine	3.25	4.81	7.72	5.6
Liver	1.33	1.62	2.09	1.9
Kidney	1.58	2.29	3.00	3.0
Pancreas	1.15	1.50	1.87	1.5
Spleen	1.21	1.45	2.33	1.4
Stomach	1.23	1.44	1.90	1.8
Thyroid	1.17	1.31	1.46	1.7
Trachea & Bronchi	1.14	1.23	1.36	1.5
Organs outside CT scan range				
Bladder	1.58	1.83	2.47	3.2
Brain	1.98	2.21	2.39	3.6
Eyes	1.29	1.38	1.53	1.9
Gall Bladder	1.15	1.54	2.30	1.7
Larynx & Pharynx	1.37	2.06	2.85	1.9
Ovaries*	1.39	1.51	1.68	
Prostate*	1.61	2.08	3.07	2.8
Small Intestine	2.80	3.54	4.81	6.2
Testes*	2.37	3.44	4.85	8.8
Uterus*	1.47	1.68	1.84	--
Distributed organs				
Bones	1.30	2.56	5.51	
Skin	5.74	6.74	7.75	--

Table 10: Ratios of 95th percentile dose to mean dose per organ, for adult abdominopelvic CT scan simulations on 58 adult XCAT phantoms

Organ/structure	Min	Average	Max
Organs completely within CT scan range			
Adrenals	1.07	1.12	1.26
Bladder	1.11	1.26	1.43
Gall Bladder	1.11	1.25	1.41
Kidneys	1.15	1.22	1.35
Large Intestine	1.25	1.37	1.56
Liver	1.30	1.37	1.48
Ovaries*	1.07	1.12	1.22
Pancreas	1.08	1.15	1.29
Prostate*	1.04	1.08	1.11
Small Intestine	1.24	1.38	1.53
Spleen	1.16	1.30	1.42
Stomach	1.21	1.35	1.56
Uterus*	1.07	1.18	1.30
Organs partially within CT scan range			
Esophagus	1.67	2.45	4.17
Heart	1.29	1.52	2.19
Lungs	1.58	2.51	3.89
Testes*	1.20	1.58	2.36
Trachea & Bronchi	2.01	3.38	4.32
Organs outside CT scan range			
Brain	2.07	2.65	3.23
Breast*	1.35	2.69	5.67
Eyes	1.55	2.07	2.59
Larynx & Pharynx	1.44	1.63	1.90
Thymus	1.32	1.71	2.35
Thyroid	1.28	1.41	1.59
Distributed organs			
Bones	1.30	3.10	11.92
Skin	4.01	4.66	5.32

Table 11: Ratios of 95th percentile dose to mean dose per organ, for pediatric chest CT scan simulations on 56 pediatric XCAT phantoms

Organ/structure	Min	Average	Max
Organs completely within CT scan range			
Breast*	1.00	1.42	1.96
Heart	1.12	1.17	1.30
Lungs	1.19	1.26	1.35
Thymus	1.08	1.16	1.24
Organs partially within CT scan range			
Adrenals	1.10	1.24	1.75
Esophagus	1.10	1.14	1.23
Liver	1.31	1.56	1.87
Spleen	1.16	1.38	1.91
Stomach	1.14	1.40	2.42
Thyroid	1.15	1.26	1.47
Trachea & Bronchi	1.13	1.18	1.34
Organs outside CT scan range			
Bladder	1.39	1.78	2.40
Brain	2.02	2.31	2.78
Gall Bladder	1.12	1.66	2.35
Eyes	1.31	1.36	1.45
Kidneys	1.45	2.44	3.02
Large Intestine	2.72	4.56	6.48
Larynx & Pharynx	1.15	1.44	2.50
Ovaries*	1.20	1.42	1.90
Pancreas	1.21	1.79	3.00
Prostate*	1.28	1.73	2.52
Small Intestine	2.85	3.65	4.59
Testes*	1.43	2.19	3.88
Uterus*	1.24	1.66	2.28
Distributed organs			
Bones	1.23	2.96	11.60
Skin	5.28	6.78	7.96

Table 12: Ratios of 95th percentile dose to mean dose per organ, for pediatric abdominal CT scan simulations on 56 pediatric XCAT phantoms

Organ/structure	Min	Average	Max
Organs completely within CT scan range			
Adrenals	1.07	1.13	1.25
Bladder	1.32	1.59	2.07
Gall Bladder	1.04	1.15	1.29
Kidneys	1.13	1.19	1.24
Liver	1.22	1.30	1.42
Pancreas	1.09	1.19	1.36
Spleen	1.14	1.21	1.34
Stomach	1.12	1.25	1.42
Organs partially within CT scan range			
Esophagus	1.49	1.98	2.74
Heart	1.23	1.43	1.76
Large Intestine	1.39	1.75	2.30
Lungs	1.47	2.04	3.21
Trachea & Bronchi	1.63	2.49	3.53
Small Intestine	1.26	1.37	1.63
Organs outside CT scan range			
Brain	2.02	2.34	3.04
Breast*	1.02	1.95	4.95
Eyes	1.35	1.57	2.01
Larynx & Pharynx	1.39	1.54	1.70
Ovaries*	1.18	1.26	1.52
Prostate*	1.16	1.24	1.39
Testes*	1.19	1.36	1.72
Thymus	1.20	1.69	3.05
Thyroid	1.25	1.38	1.50
Uterus*	1.23	1.42	1.69
Distributed organs			
Bones	1.18	2.78	11.56
Skin	4.91	6.27	7.50

R95 values were also plotted as a function of equivalent diameter and average organ distance from the center of the phantom, but trends were inconsistent. Most organs did not show a strong correlation between heterogeneity and either average organ distance or effective patient diameter. The only compelling result was R95 versus the average organ distance of the skin. Figure 11 shows the results of R95 versus average organ distance for the skin in abdominopelvic and chest CT protocols of both adults and pediatric phantoms. The colored lines show linear regression fits with the following results: for the abdominopelvic simulations, $R^2=0.81$, $p<0.0001$; and for the chest simulations, $R^2=0.76$, $p<0.0001$.

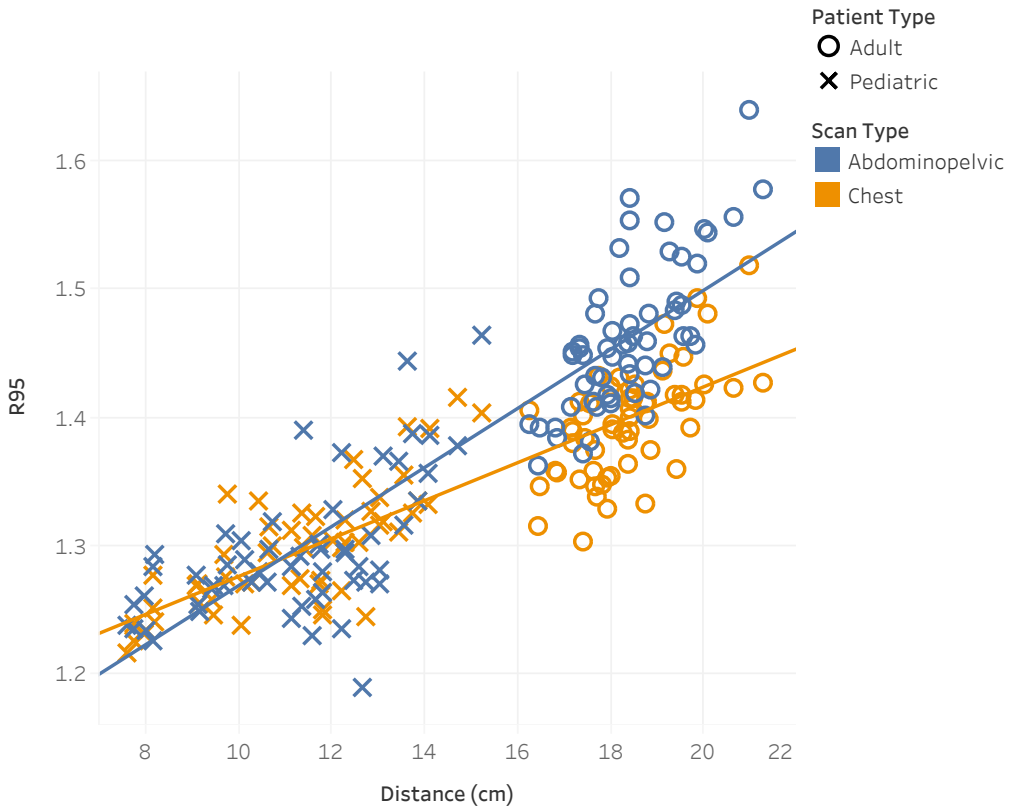

Figure 11: Ratio of 95th percentile dose to mean dose for the skin (R95), for each patient and protocol considered in this study. The x-axis gives the average distance of skin from the mass-weighted axial centroid of each patient.

Next, we calculated the absorbed dose values obtained when using all the voxels in organ versus only the voxels within the scan limits. Figure 12 shows the average in-field dose divided by the average dose to the entire organ plotted against the function of the organ within the beam. We have further separated the data into two categories, distributed organs (bones, skin, and marrow) and all other organs.

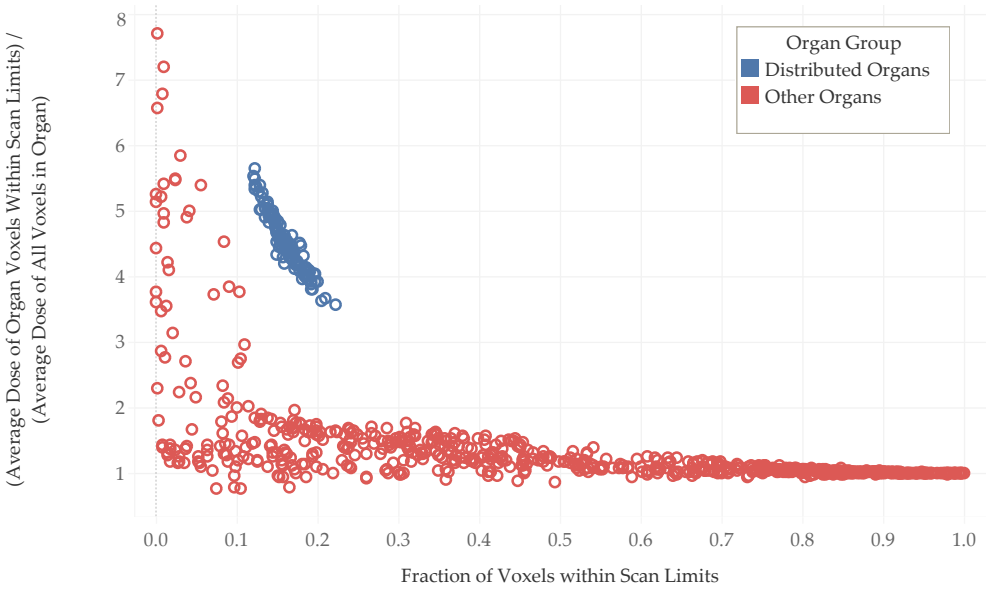

Figure 12: Average in-field dose divided by the total average dose for each organ as a function of fraction of voxels in the scan limits, for the given organ. Results are grouped into distributed organs (bones, marrow, and skin) and all other organs

3.3.3 Effect of Scan Parameters

To investigate the effect of pitch and projections per rotation, we first compared the average organ doses using a pitch of 0.6 and 1.375 for a single adult abdominopelvic scan. The absorbed dose did not differ by more than 0.51% for any given organ. Next, organ doses were compared for the same scan and patient, using 36 projections per rotation and 180 projections per rotation. For this comparison, there was no difference between any of the organ doses at the level of precision recorded by MCGPU.

Similarly, we examined the effect of pitch and number of projections on the volumetric distribution of dose. Using a pitch of 1.375 versus 0.6 changed R95 by no

more than 0.79% and using 180 vs 36 projections per rotation had no measureable effect on R95. Furthermore, DVHs showed only very small qualitative differences in dose volume distribution. As an example, the dose volume histogram for the organ with the largest percent difference in dose volume characteristics (eyes) is shown below. It should be noted that these doses are very small compared to the typical doses to organs within the beam, which are in the range of 1.9 – 53.7 mGy / (mAs per rot).

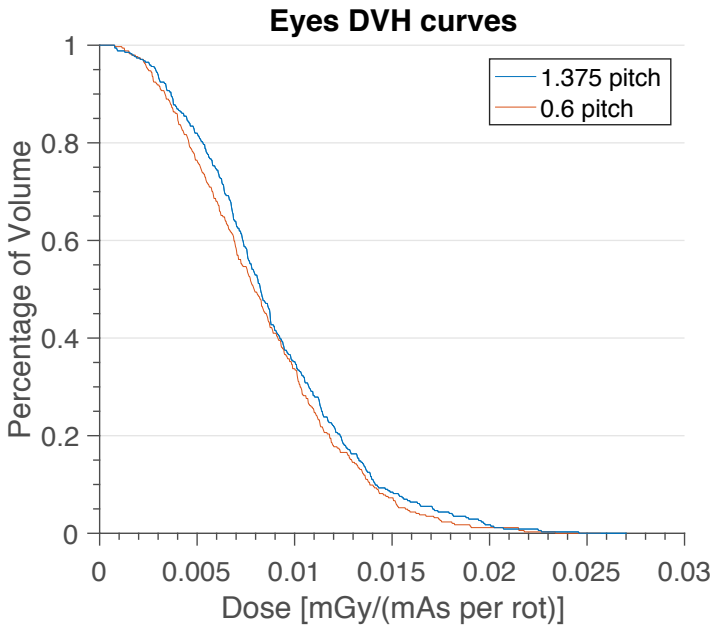

Figure 13: Dose-volume histograms from a simulated pitch of 0.6 and 1.375, for a single adult abdominopelvic protocol. The y axis shows the fraction of volume that receives at least a given dose value.

3.3.4 Tissue Weighted Dose Models

In the Figure 14, we show the results of the effective dose, equivalent full-field dose (EFD), and equivalent in-field dose (EID), as a function of effective patient diameter. As in the previous section, the absorbed dose has been normalized to a constant tube output of 100 mAs per rotation.

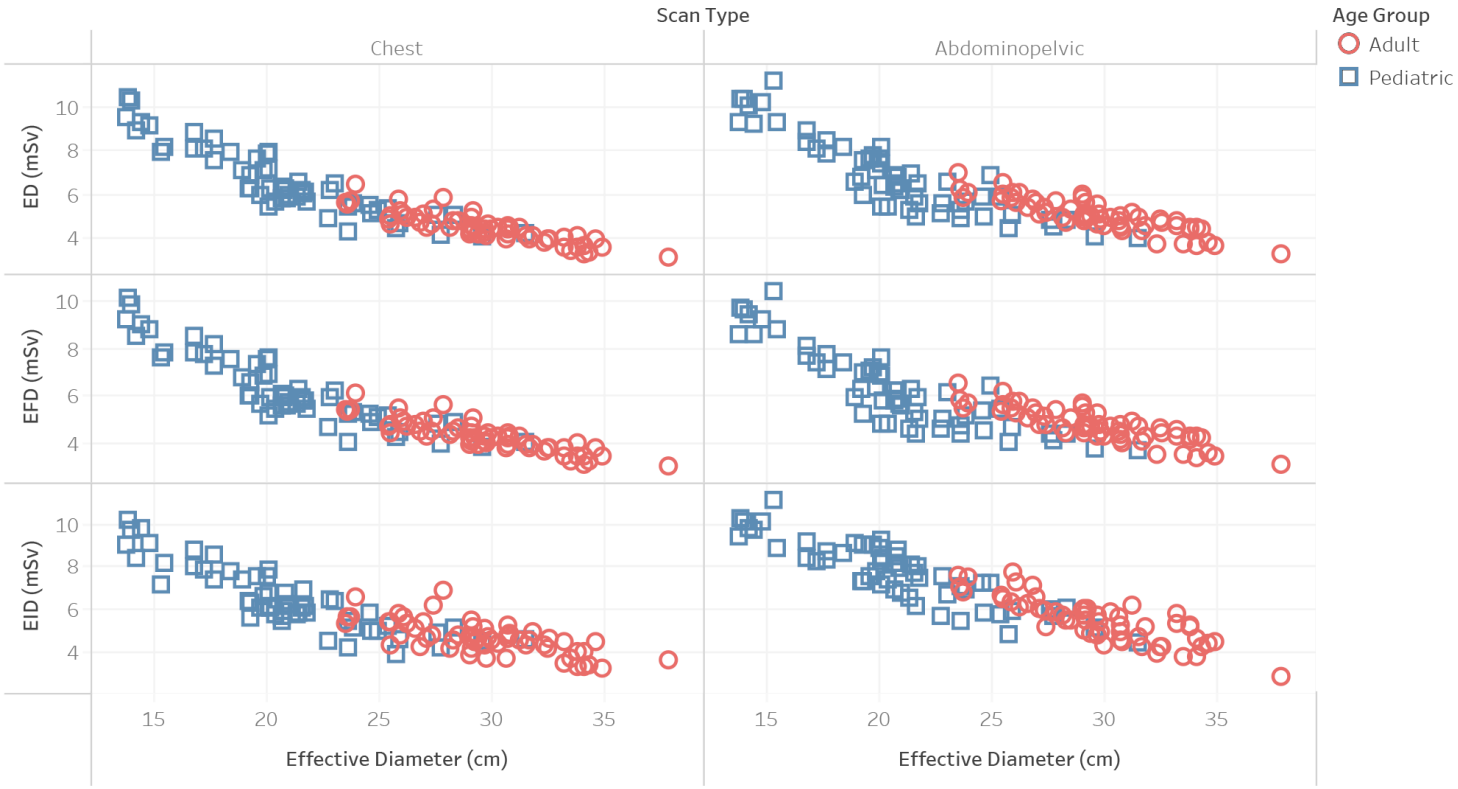

Figure 14: Tissue-weighted dose calculations as a function of effective diameter for abdominopelvic and chest CT scans for both adult and pediatric phantoms. Dose results are normalized to a constant tube output of 100 mAs per rotation. ED is effective dose. EFD is equivalent full-field dose, which uses all voxels in all organs to calculate absorbed doses. EID is equivalent in-field dose, which considers only voxels within the scan limits.

In Table 13, we show the average results of the different tissue-weighted dose models across all patients in each scan type. The traditional effective dose (ED) values are given in mSv, while the EFD, EID, and EDQ averages are shown as a ratio relative to the ED values.

Table 13: Comparison of different tissue-weighted dose equivalency models

Scan Protocol	ED[a] (mSv)	EFD[b] ED	EID[c] ED	EDQ_1[d] ED	EDQ_2 ED	EDQ_3 ED	EDQ_4 ED	EDQ5 ED
Ped. Chest (n=56)	6.59	0.96	0.99	0.61	0.79	0.94	1.08	1.36
Ped. Abd. Pelv. (n=56)	6.83	0.91	1.15	0.44	0.64	0.88	1.13	1.45
Adult Chest (n=58)	4.46	0.95	1.04	0.57	0.76	0.92	1.09	1.43
Adult Abd. Pelv. (n=58)	5.02	0.94	1.09	0.59	0.70	0.85	1.10	1.47

[a]effective dose, averaged across all patients each category
[b]equivalent full-field dose, which uses all dose voxels for all organs
[c]equivalent in-field dose, which uses only dose voxels within scan limits
[d]equivalent dose quintile, uses only the N^{th} quintile of dose voxels in each organ

3.4 Discussion

For the adult chest CT scans, we see that the dose heterogeneity results were in general agreement with Samei et al.,[42] particularly for organs fully within the CT scan range. Evaluating all the scans studied in this work, the heterogeneity ratios did not exceed 2.19 for organs fully in the scan range. However, for organs outside the scan range, the heterogeneity ratios were as high as 11.92. For these organs, this means that approximately 5% of the volume was receiving ≥11 times the mean dose of that organ. This is not surprising for larger organs such as the skin, bones, or intestines, where a

small portion of the organ may be in the primary beam while a larger portion may be far from the beam. For most of the organs, plots of heterogeneity ratio vs effective diameter showed weak or conflicting trends between simulations. Some organs may have shown little correlation to effective diameter because they were near the periphery of the body habitus, so that the lateral tissue attenuation distance did not significantly change with effective diameter. Alternatively, for those organs that were uniformly irradiated, it made sense that we should not see a meaningful correlation between heterogeneity with effective diameter.

However, we see that the R95 showed a strong correlation with the average distance of skin from the center of the phantom. This was because a larger patient would have the same peak skin dose (for a given tube output) but the average dose would be distributed over a larger area. Thus, the mean dose would decrease, but the peak dose would remain the same.

Next we calculated dose to each organ of each patient and scan using either: (a) only voxels within the scan limits, or (b) all the voxels in the given organ. When we plotted the ratio of (a) to (b) as a function of the fraction of the organ within the scan limits, we saw an inverse power relationship. For some organs with only a small fraction in the field, we saw changes in dose of up to 8-fold. To explain this, we consider a rough example case, for a uniform rod in a uniform parallel radiation field (see Figure 15).

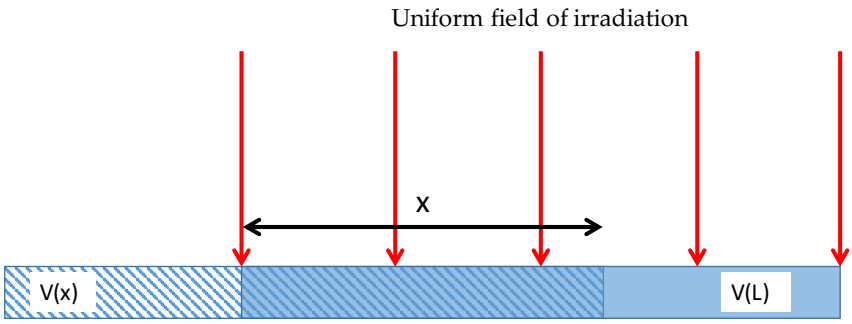

Figure 15: Comparison of a volume fully within an irradiation field versus a volume only partially within the field. Here, x indicates the length of the volume that is in the field.

In this case, V(L) is the unshifted volume fully within the field of irradiation, V(x) is the volume shifted such that a length x is still within the field. For a given x value, we expect that the dose within the field should remain the same. However, the average dose to the *total* shifted volume V(x) should decrease linearly with the proportion of the volume outside of the field, which is also proportional to x. Thus, the ratio of in-field dose to the average dose should decrease as 1/x. This was generally in accordance with what we see as a bounding envelope for Figure 12. The dose did not follow this trend exactly, because organs may have received differential scatter based on their location within the body, relative to the ends of the scan. Furthermore, an organ being within the scan limits did not necessarily mean that it was uniformly irradiated, because of the striping pattern that occured with helical scans (see Figure 10). We also saw that the results are different for distributed organs such as bones and skin; for a given fractional irradiation volume, these organs showed a greater difference between in-field and full-

field organ dose. This was most likely because these distributed organs take up significantly more volume than the typical organs. The size of the organ can extend to the point where even though a large fraction is within the beam, the portion outside of the beam can extend beyond the scattering distance. Therefore, the whole-organ average dose would decrease relative to the same in-field dose. Still, the same general trend was seen for these distributed organs.

Next, we considered the effect of pitch and projections per rotation on the heterogeneity results. For the change in pitch, we found that the average organ doses did not change by more than 0.5% and the dose heterogeneity (R95) values did not change by more than 0.79%. Furthermore, the most drastic difference between organ dose volume characteristics was shown for the eyes (figure 12), but this was still a very small dosimetric difference when compared to the average organ doses. Furthermore, this was for an organ far outside the field of radiation. For organs within the field, the dose volume histograms could not be distinguished between each other. When considering the number of projections, the number of projections per rotation had no detectable effect on average dose, R95, or dose volume histogram results.

Following these in-field and full-organ dose measures, we considered different methods for calculating tissue-weighted dose parameters, inspired by the calculations of effective dose. The reference effective dose (ED) was taken to be the case where only

dose within the field of irradiation was used for skin and bones, but the whole organ dose was used for other organs. When plotting effective dose (ED) alongside the equivalent in-field dose (EID) and equivalent full-field dose (EFD) as a function of effective diameter (Figure 14) we did not see qualitative changes in the overall shape or range of the distribution. However, when we take the ratio of ED to EFD or EID (Table 13), we found relative changes of -9% to +15% from unity. Compared to the range of equivalent dose quintiles (EDQ) values, we found that EFD and EID values fell within the 3rd and 4th equivalent dose quintiles, within the statistical uncertainty. This suggested that the associated "error bars" for effective dose can be on the order of the difference between the 3rd and 4th equivalent dose quintiles. These differences would likely occur if measurements were taken in the field and compared a simulation that took the whole organ into account, especially in the case where the dose was not homogenous. In terms of percent change, this was only plus or minus 13% from unity and may well be within the uncertainty of effective dose risk calculations. A full discussion of the uncertainties associated with risk coefficients was outside the scope of this thesis, but is described elsewhere.[53] Nonetheless, it was found that dose heterogeneity can change the results of simulated effective dose in CT scans.

There were several limitations to this study including the small number of CT scan types. Furthermore, risk coefficients were generalized to the population average

and only roughly considered age or gender in the calculation of bone marrow dose. More intricate models could further refine the tissue-weighted dose quantities across patient sizes, in the context of dose heterogeneity. A more detailed microstructure model of bone could also expand upon the dose heterogeneity results for bone marrow and surface and their influence on tissue-weighted dose quantities.

4. Conclusion

Organ dose heterogeneity characteristics were calculated from the results of Monte Carlo simulations for chest and abdominopelvic CT scans across 58 adult phantoms and 56 pediatric phantoms. For some organs in this study, the 95th percentile dose was over 11 times the mean organ dose. We also found that the difference between in-field dose and total average dose for a given organ can vary by as much as a factor of 8, with this difference decreasing as the fractional irradiation of the organ approaches unity. When calculating effective doses using only dose voxels within the radiation field versus the entire organ, we found that the effective dose results change by as much as 13%. The results have shown that dose-volume details may be hidden by average dose estimates and suggest the need to consider intra-organ dose heterogeneity in CT dose calculations, particularly in the case of sensitive tissues (e.g., bone marrow) and populations (e.g., pediatric).

References

1. NCRP. Ionizing radiation exposure of the population of the United States. *Natl Counc Radiat Prot Meas*. 2009;Report 160.

2. Balagué F, Mannion AF, Pellisé F, Cedraschi C. Non-specific low back pain. *Lancet*. 2012;379(9814):482-491. doi:https://doi.org/10.1016/S0140-6736(11)60610-7.

3. Vos T, Flaxman AD, Naghavi M, et al. Years lived with disability (YLDs) for 1160 sequelae of 289 diseases and injuries 1990-2010: A systematic analysis for the Global Burden of Disease Study 2010. *Lancet*. 2012;380(9859):2163-2196. doi:10.1016/S0140-6736(12)61729-2.

4. Manchikanti L, Pampati V, Hirsch JA. Retrospective cohort study of usage patterns of epidural injections for spinal pain in the US fee-for-service Medicare population from 2000 to 2014. *BMJ Open*. 2016;6(12):e013042. doi:10.1136/bmjopen-2016-013042.

5. Manchikanti L, Pampati V, Falco FJE, Hirsch JA. Growth of spinal interventional pain management techniques: Analysis of utilization trends and medicare expenditures 2000 to 2008. *Spine (Phila Pa 1976)*. 2013;38(2):157-168. doi:10.1097/BRS.0b013e318267f463.

6. Weinstein SM, Herring SA. Lumbar epidural steroid injections. *Spine J*. 2003;3:37-44. doi:10.1016/S1529-9430(02)00560-0.

7. Bogduk N. Practice guidelines for spinal diagnostic and treatment procedures. In: *International Spine Intervention S.* ; 2013.

8. McCormick ZL, Mattie R, Ebrahimi A, et al. Is There a Relationship Between Body Mass Index and Fluoroscopy Time During Cervical Interlaminar Epidural Steroid Injections? *PAIN Med*. 2017;18(7):1326-1333. doi:10.1093/pm/pnw264.

9. Kranz PG, Raduazo P, Gray L, Kilani RK, Hoang JK. CT fluoroscopy-guided cervical interlaminar steroid injections: Safety, technique, and radiation dose parameters. *Am J Neuroradiol*. 2012;33(7):1221-1224. doi:10.3174/ajnr.A2954.

10. McCormick ZL, Choxi SC, Lee DT, et al. The Impact of Body Mass Index on Fluoroscopy Time During Lumbar Epidural Steroid Injection; A Multicenter

Cohort Study. *PAIN Med*. 2017;18(1):25-35. doi:10.1093/pm/pnw050.

11. Cushman D, Mattie R, Curtis B, Flis A, McCormick ZL. The effect of body mass index on fluoroscopic time and radiation dose during lumbar transforaminal epidural steroid injections. *SPINE J*. 2016;16(7):876-883. doi:10.1016/j.spinee.2016.03.041.

12. Cushman DM, Mattie R, Clements ND, McCormick ZL. The Effect of Body Mass Index on Fluoroscopic Time and Radiation Dose During Intra-articular Hip Injections. *PM R*. 2016;8(9):876-882. doi:10.1016/j.pmrj.2016.01.011.

13. Cushman D, Flis A, Jensen B, McCormick Z. The Effect of Body Mass Index on Fluoroscopic Time and Radiation Dose During Sacroiliac Joint Injections. *PM&R*. 2016;8(8):767-772. doi:10.1016/j.pmrj.2015.11.008.

14. Smuck M, Zheng P, Chong T, Kao M-C, Geisser ME. Duration of Fluoroscopic-Guided Spine Interventions and Radiation Exposure Is Increased in Overweight Patients. *PM R*. 2013;5(4):291-296. doi:10.1016/j.pmrj.2013.01.015.

15. Hoang JK, Yoshizumi TT, Toncheva G, et al. Radiation dose exposure for lumbar spine epidural steroid injections: A comparison of conventional fluoroscopy data and CT fluoroscopy techniques. *Am J Roentgenol*. 2011;197(4):778-782. doi:10.2214/AJR.10.6102.

16. Plastaras C, Appasamy M, Sayeed Y, et al. Fluoroscopy Procedure and Equipment Changes to Reduce Staff Radiation Exposure in the Interventional Spine Suite. *Pain Physician*. 2013;16(6):E738. http://duke.summon.serialssolutions.com/2.0.0/link/0/eLvHCXMwpV3LitswFBUzpZRCKX1P-gAtSjfBxbJsy1p0EYLDBJohxNNCV4MsS22gk7gzNjT_0w-tXlbsMIuUbkyiGGN0T3SPpHuOAMDRxzA4GBMIy1AqY0W2pcKIJIkgUZzQuKpSmUpj_tnTiJ386aQxd0utXLnzfwdctamQawHtPwTdP1Q1qM8q9Oqqgq-uR4V_9rPdaq.

17. The 2007 Recommendations of the International Commission on Radiological Protection. ICRP publication 103. *Ann ICRP*. 2007;37(2-4):1-332. doi:10.1016/j.icrp.2007.10.003.

18. CDC. About Adult BMI. Healthy Weight. https://www.cdc.gov/healthyweight/assessing/bmi/adult_bmi/index.html. Published 2017.

19. Segars WP, Sturgeon G, Mendonca S, Grimes J, Tsui BMW. 4D XCAT phantom for multimodality imaging research. *Med Phys*. 2010;37(9):4902-4915. doi:10.1118/1.3480985.

20. White DR, Griffith R V, Wilson IJ. Report 46. *J Int Comm Radiat Units Meas*. 1992;os24(1):NP-NP. http://dx.doi.org/10.1093/jicru/os24.1.Report46.

21. Bair WJ, Kellerer A, Stannard JN, Thompson RC. Report No. 046 - Alpha-Emitting Particles in Lungs. *J Natl Counc Radiat Prot Meas*. 1975.

22. Cristy M, Eckerman KF. Specific Adsorbed Fractions of Energy at Various Ages From Internal Photon Sources. *Ornl/Tm-8381 V1-V7*. 1987. doi:10.1.1.453.354.

23. Li X, Samei E, Segars WP, et al. Patient-specific radiation dose and cancer risk estimation in CT: Part I. Development and validation of a Monte Carlo program. *Med Phys*. 2011;38(1):397-407. doi:10.1118/1.3515839.

24. Agostinelli S, Allison J, Amako K, et al. Geant4—a simulation toolkit. *Nucl Instruments Methods Phys Res Sect A Accel Spectrometers, Detect Assoc Equip*. 2003;506(3):250-303. doi:https://doi.org/10.1016/S0168-9002(03)01368-8.

25. Alnewaini Z, Langer E, Schaber P, et al. Real-time, ray casting-based scatter dose estimation for c-arm x-ray system. *J Appl Clin Med Phys*. 2017;18(2):144-153. doi:10.1002/acm2.12036.

26. Carver DE, Kost SD, Fernald MJ, et al. Development and validation of a GEANT4 radiation transport code for CT dosimetry. *Health Phys*. 2015;108(4):419-428. doi:10.1097/HP.0000000000000243.

27. Poon E, Verhaegen F. Accuracy of the photon and electron physics in GEANT4 for radiotherapy applications. *Med Phys*. 2005;32(6Part1):1696-1711. doi:10.1118/1.1895796.

28. Maigne COT and VB and DD and BH and L. Validation of a dose deposited by low-energy photons using GATE/GEANT4. *Phys Med Biol*. 2008;53(11):3039. http://stacks.iop.org/0031-9155/53/i=11/a=019.

29. Ventura DLP and DB and FL and CP and SA and GAPC and VG and EL and NR and FR and GVR and VS and CS and C. A real-time, large area, high space resolution particle radiography system. *J Instrum*. 2014;9(6):C06012.

http://stacks.iop.org/1748-0221/9/i=06/a=C06012.

30. Darambara MEM and MZ and DG. Normalized mean glandular dose computation from mammography using GATE: a validation study. *Phys Med Biol*. 2013;58(7):2247. http://stacks.iop.org/0031-9155/58/i=7/a=2247.

31. Sechopoulos I, Ali ESM, Badal A, et al. Monte Carlo Reference Data Sets for Imaging Research: The Report of AAPM Task Group 195. *Med Phys*. 2015;42(10):5679-5691. doi:10.1118/1.4928676.

32. Punnoose J, Xu J, Sisniega A, Zbijewski W, Siewerdsen JH. Technical Note: SPEKTR 3.0-A computational tool for x-ray spectrum modeling and analysis. *Med Phys*. 2016;43(8):4711-4717. doi:10.1118/1.4955438.

33. Angthong C, Adams SB, Easley ME, DeOrio JK, Nunley JA. Radiation exposure in total ankle replacement. *Foot ankle Int*. 2014;35(11):1131-1136.

34. Lee C, Lee C, Shah AP, Bolch WE. An assessment of bone marrow and bone endosteum dosimetry methods for photon sources. *Phys Med Biol*. 2006;51(21):5391-5407. doi:10.1088/0031-9155/51/21/001.

35. King SD, Spiers FW. Photoelectron Enhancement of the Absorbed Dose from X Rays to Human Bone Marrow: Experimental and Theoretical Studies. *Br J Radiol*. 1985;58(688):345-356. doi:10.1259/0007-1285-58-688-345.

36. Cristy M. Active bone marrow distribution as a function of age in humans. *Phys Med Biol*. 1981;26(3):389. http://stacks.iop.org/0031-9155/26/i=3/a=003.

37. Kim S, Toncheva G, Anderson-Evans C, Huh BK, Gray L, Yoshizumi T. Kerma Area Product Method for Effective Dose Estimation During Lumbar Epidural Steroid Injection Procedures: Phantom Study. *Am J Roentgenol*. 2009;192(6):1726-1730. doi:10.2214/AJR.08.1713.

38. Huda W. Kerma-Area Product in Diagnostic Radiology. *Am J Roentgenol*. 2014;203(6):W565-W569. doi:10.2214/AJR.14.12513.

39. Abbott ZI, Nair K V, Allen RR, Akuthota VR. Utilization characteristics of spinal interventions. *Spine J*. 2012;12(1):35-43. doi:10.1016/j.spinee.2011.10.005.

40. Leung KC, Martin CJ. Effective doses for coronary angiography. *Br J Radiol*.

1996;69(821):426-431. doi:10.1259/0007-1285-69-821-426.

41. Vilar-Palop J, Vilar J, Hernández-Aguado I, González-Alvarez I, Lumbreras B. Updated effective doses in radiology. *J Radiol Prot*. 2016;36(4):975-990. doi:10.1088/0952-4746/36/4/975.

42. Samei E, Li X, Chen B, Reiman R. The effect of dose heterogeneity on radiation risk in medical imaging. *Radiat Prot Dosimetry*. 2013;155(1):42-58. doi:10.1093/rpd/ncs275.

43. Badal A, Badano A. Accelerating Monte Carlo simulations of photon transport in a voxelized geometry using a massively parallel graphics processing unit. *Med Phys*. 2009;36(11):4878-4880. doi:10.1118/1.3231824.

44. Sharma S, Kapadia A, Abadi E, Fu W, Segars WP, Samei E. A rapid GPU-based Monte Carlo simulation tool for individualized dose estimations in CT. In: *Proc. SPIE 10573, Medical Imaging 2018*. ; 2018:Manuscript Submitted for Publication.

45. Smith-Bindman R, Lipson J, Marcus R, Al E, Investigation O. Radiation dose associated with common computed tomography examinations and the associated lifetime attributable risk of cancer. *Arch Intern Med*. 2009;169(22):2078-2086. http://dx.doi.org/10.1001/archinternmed.2009.427.

46. Tian X, Li X, Segars WP, Paulson EK, Frush DP, Samei E. Pediatric Chest and Abdominopelvic CT: Organ Dose Estimation Based on 42 Patient Models. *Radiology*. 2014;270(2):535-547. doi:10.1148/radiol.13122617.

47. Kalra MK, Maher MM, Toth TL, et al. Techniques and Applications of Automatic Tube Current Modulation for CT. *Radiology*. 2004;233(3):649-657. doi:10.1148/radiol.2333031150.

48. Boone JM, Strauss KJ, Cody DD, McCollough CH, McNitt-Gray MF, Toth TL. Size-specific dose estimates (SSDE) in pediatric and adult body CT exams. *Rep AAPM Task Gr 204*. 2011.

49. Drzymala RE, Mohan R, Brewster L, et al. Dose-volume histograms. *Int J Radiat Oncol Biol Phys*. 1991;21(1):71-78. doi:10.1016/0360-3016(91)90168-4.

50. Zhang Y, Li X, Paul Segars W, Samei E. Organ doses, effective doses, and risk indices in adult CT: Comparison of four types of reference phantoms across

different examination protocols. *Med Phys*. 2012;39(6):3404-3423. doi:10.1118/1.4718710.

51. Zhang Y, Li X, Segars WP, Samei E. Comparison of patient specific dose metrics between chest radiography, tomosynthesis, and CT for adult patients of wide ranging body habitus. *Med Phys*. 2014;41(2):23901. doi:10.1118/1.4859315.

52. Li X, Samei E, Segars WP, Sturgeon GM, Colsher JG, Frush DP. Patient-specific Radiation Dose and Cancer Risk for Pediatric Chest CT. *Radiology*. 2011;259(3):862-874. doi:10.1148/radiol.11101900.

53. Wakeford MP and WZ and JDH and R. Assessing the reliability of dose coefficients for exposure to radioiodine by members of the public, accounting for dosimetric and risk model uncertainties. *J Radiol Prot*. 2017;37(2):506. http://stacks.iop.org/0952-4746/37/i=2/a=506.